Two-phase magma flow with phase exchange -Part II -1.5D numerical simulations of a volcanic conduit

Alain Burgisser, Marielle Collombet, Gladys Narbona-Reina, Didier Bresch

Two-phase magma flow with phase exchange
– Part II –
1.5D numerical simulations of a volcanic conduit

Alain Burgisser*, Marielle Collombet*, Gladys Narbona-Reina†, Didier Bresch‡

July 7, 2024

Abstract

In a review paper in this same volume, we present the state of the art on modeling of compressible viscous flows ranging from single-phase to two-phase systems. It focuses on mathematical properties related to weak stability because they are important for numerical resolution and on the homogenization process that leads from a microscopic description of two separate phases to an averaged two-phase model. This review serves as the foundation for Parts I and II, which present averaged two-phase models with phase exchange applicable to magma flow during volcanic eruptions. Part I establishes a two-phase transient conduit flow model ensuring: 1) mass and volatile species conservation, 2) disequilibrium degassing considering both viscous relaxation and volatile diffusion, and 3) dissipation of total energy. The relaxation limit of this model is then used to obtain a drift-flux system amenable to simplification. Here, in Part II, we summarize this model and propose a 1.5D simplification of it that alleviates three issues causing difficulties in its numerical implementation. We compare our model outputs to those of another steady-state, equilibrium degassing, isothermal model under conditions typical of an effusive eruption at an andesitic volcano. Perfect equilibrium degassing is unreachable with a realistic water diffusion coefficient because conduit extremities always contain melt supersaturated with water. Such supersaturation has minor consequences because results show that assuming equilibrium degassing has a small influence on mass discharge rate. In contrast, releasing the isothermal assumption reduces significantly mass discharge rate by cooling due to gas expansion, which in turn increases liquid viscosity. We propose a simplified system using Darcy's law and omitting several processes such as shear heating and liquid inertia. This minimal system is not dissipative but approximates the steady-state mass discharge rate of the full system within 10%. A regime diagram valid under a limited set of conditions indicates when this minimal system captures the ascent dynamics of effusive eruptions. Interestingly, the two novel aspects of the full model, diffusive degassing and heat balance, cannot be neglected. In some cases with high diffusion coefficients, a shallow region where porosity and velocities tend towards zero develops initially, possibly blocking an eventual steady state. This local porosity loss also occurs when a steady-state solution is subjected to a change in shallow permeability. The resulting shallow porosity loss features many characteristics of a plug developing prior to a Vulcanian eruption.

*Univ. Grenoble Alpes, Univ. Savoie Mont Blanc, CNRS, IRD, Univ. Gustave Eiffel, ISTerre, 38000 Grenoble, France, alain.burgisser@univ-smb.fr, marielle.collombet@univ-smb.fr

†Dpto. Matemática Aplicada I E.T.S Arquitectura, Universidad de Sevilla, Avda. Reina Mercedes N.2, 41012 Sevilla, Spain,gnarbona@us.es

‡LAMA UMR5127 CNRS, Batiment 21, Université Savoie Mont Blanc, 73376 Le Bourget du lac, France, didier.bresch@univ-smb.fr

Contents

1 Introduction

The diversity of volcanic eruptive regimes, from gas-rich, particle-laden jets to slow effusion of gas-poor lavas, is a direct consequence of the multiphase nature of magmas, which are composed of silicate liquid, crystals, and a compressible fluid that can be either a gas or a supercritical fluid. This diversity, which has not yet been rationalized in a single physical framework, led early modeling attempts to focus on end-member cases. [Wilson, 1980], for instance, described explosive, gas-rich eruptions with the energy equation of an expanding gas to relate gas pressure to ejection velocity. The propelling volcanic gas, however, is made of volatile species that, at depth, are either dissolved into the silicate liquid or present as individual gas bubbles. The eruptive regime depends greatly on how these volatiles come out of solution during the ascent towards the surface to form a continuous gas phase. The changes in pressure and temperature

due to the ascent deeply affect the relative proportions of silicate liquid, crystals, and gas, and a thorough review of the associated physical processes can be found in [Gonnermann and Manga, 2007].

Quickly [Wilson and Head, 1981], gas-based models were complemented by models of volcanic conduit flow based on the mass and momentum conservations of a single-phase magma where gas bubbles, silicate liquid, and crystals are represented by a Navier-Stokes equation with Boussinesq approximation along a one-dimensional cylindrical conduit assuming a parabolic velocity distribution across the conduit (often referred to as the 1.5D approximation) (e.g., [Jaupart and Allègre, 1991]; [Papale and Dobran, 1993]; [Woods, 1995]; [Survey et al., 2000]; [Michaut et al., 2013]). The single-phase assumption was motivated by the high viscosity of most silicate liquids, which restricts the motion of crystals and bubbles relative to the liquid. While this relative immobility holds for individual gas bubbles, it does not accurately represent the observed tendencies of bubbles to coalesce and form an interconnected network permeable to the gas they contain. Considering magma as a single-phase fluid also leads to an unavoidable separation of the Strombolian and Vulcanian regimes (based on the free escape of gas bubbles from essentially immobile magma) and the Plinian regime (based on the immobility of bubbles relative to the magmatic liquid), precluding the study of the frequent transitions between these regimes observed during a single eruptive event [Slezin, 2003]. These considerations led to the introduction of a second set of Navier-Stokes equations for the gas phase, thus constituting a two-phase system with mass exchange ([Yoshida and Koyaguchi, 1999]; [Kozono and Koyaguchi, 2009]; [Degruyter et al., 2012]; [La Spina and de' Michieli Vitturi, 2012]; [Fowler and Robinson, 2018]). In such two-phase systems, the other phase represents an ideal mixture of crystals suspended into a silicate liquid.

The effect of mass exchange is far from trivial because it reinforces the effect of gas expansion during ascent, causing gas volume fraction to span the entire range between 0 and 1. Note that the nucleation of gas bubbles, which is not directly addressed in this work, owes a lot of its complexity to the presence of crystals that act as nucleation sites (e.g., [Shea, 2017]. Since the pioneering work of [Sparks, 1978], the growth dynamics of bubbles nucleated in viscous liquids has been explored in depth experimentally (e.g. among our works: [Burgisser and Gardner, 2004]; [Castro et al., 2012]) and with numerical models (e.g. [Coumans et al., 2020] ; [Forestier-Coste et al., 2012], [Mancini et al., 2016]; [Huber et al., 2014]; [Su and Huber, 2017]). These studies demonstrated that growth occurs under the combined effect of volatile diffusion from the liquid into the bubble and of the viscous relaxation of the spherical bubble due to gas compressibility. Integrating these two microscopic growth processes into a macroscopic description of the flowing magma has been surprising difficult. Leaving viscous relaxation aside, [Mason et al., 2006] incorporated diffusion degassing with an analytical diffusion equation valid at small Peclet number into a single-phase flow and [Lensky et al., 2008] included a quasi-static diffusion equation into a stick-slip model of shallow magma plug.

Instead, most models assume thermodynamical equilibrium bubble growth, whether with a single phase magma (e.g., [Melnik, 2000]; [Melnik and Sparks, 2005] ; [Costa et al., 2009]), or a two-phase magma (e.g., [Kozono and Koyaguchi, 2009]; [Degruyter et al., 2012]). Such growth neglects viscous relaxation by using a single pressure that represents both gas and liquid pressures (the algebraic closure of the review paper (Section 4.2.1) and in Part I (Section 2) [Bresch et al., 2024, Narbona-Reina et al., 2024]) and assumes that the dissolved volatiles (usually water) are always at saturation. As a result, the dissolved volatile concentration is algebraically linked to pressure by, for instance, Henry's law of solubility. Although in two-phase models the gas, liquid, and total masses are conserved, this last assumption precludes mass conservation of the volatile species. An example of a two-phase flow model with a single pressure and assuming equilibrium bubble growth is that of [Degruyter et al., 2012]. We use the Degruyter model as a reference for comparison because it is regularly applied to natural cases ([Burgisser et al., 2017]; [Cassidy et al., 2018]; [Crozier et al., 2022]) and it has also been used as benchmark for a two-phase, isothermal model [Mullet and Segall, 2021].

Some warnings ([Wilson, 1998]; [Massol and Jaupart, 1999]; [Massol and Jaupart, 2009]) have been issued about the 1.5D assumption, which considers the conduit as a vertical cylinder. The transition to 2D, however, has proven to be difficult. Only a few models include gas mass exchange to date: [Dufek and Bergantz, 2005], [Dartevelle and

Valentine, 2007], [Collier and Neuberg, 2006], and [Collombet, 2009]. One of the main gain of such 2D models is the capability of studying lateral distribution of parameters such as pressure gradients, gas and heat loss at conduit walls (such as done by [Wong and Segall, 2019] in 1D for gas losses), and rheology variations caused by shear zones and shear heating.

Our aim was to establish in Part I [Narbona-Reina et al., 2024] a two-phase, three-component transient conduit flow model that ensures 1) mass and volatile species conservation, 2) disequilibrium degassing taking into account both viscous relaxation and volatile diffusion, and 3) dissipation of total energy. We did not enforce total energy conservation as some terms are negligible and thus simplify the system to be solved. The requirement of energy dissipation corresponds to the fact that we consider the magma without porous surrounding. In this work, we propose a 1.5D simplification of this model. The dimension reduction is done by assuming a parabolic Newtonian velocity distribution horizontally and it is thus sometimes referred to as a 1.5D model. We then propose a numerical implementation and a comparison with the steady-state Degruyter model that highlights to which degree our transient model recovers equilibrium degassing. We finally present a new transient behavior that emerges as a result of relaxing the dual assumption of disequilibrium degassing.

2 General model

Variable	Definition (unit)
T_g	gas temperature (K)
T_l	liquid temperature (K)
R^{H_2O}	mass exchange term (kg/m^3 s)
C_l	melt water concentration
c_{pm}, c_{pn}	bulk heat capacities (J/kg K)
c_{vg}	gas heat capacity at constant volume (J/kg K)
p_g	gas pressure (Pa)
p_l	liquid pressure (Pa)
u_g	gas velocity (m/s)
u_l	liquid velocity (m/s)
u_T	bulk heat transport velocity based on c_{pm} (m/s)
u_n	bulk heat transport velocity based on c_{pn} (m/s)
$\mathcal{D}_g$	gas viscous stress tensor (Pa)
$\mathcal{D}_l$	liquid viscous stress tensor (Pa)
D_H	shear heating (Pa/s)
K_d	drag factor (Pa s/m^2)
k	magma permeability (m^2)
Nu	Nusselt number
R_b	bubble radius (m)
Q	mass discharge rate (kg/s)

(a) Latin symbols

Variable	Definition (unit)
ρ_g	gas density (kg/m^3)
φ	gas volume fraction or porosity
η_l	liquid viscosity (Pa s)
γ	heat transfer coefficient (J/ K m^3 s)
χ	viscous factor (1/ Pa s)

(b) Greek symbols

Table 1: Main variables list. The constant parameters are listed in Table 2.

Here we present the 3D formulation of the conduit flow model that is based on that presented in Part I [Narbona-Reina et al., 2024], Section 2, which is a two-phase, three-component model for a gas and liquid mixture based on mass, momentum, and energy conservation for each phase. The subscripts l and g in variables denote the property for each

phase, liquid and gas respectively. The gas phase has only one component, water vapor. The liquid phase has two components, (dry) silicate melt and dissolved water. The unknowns of the system are the gas volume fraction φ, the gas density ρ_g, the water concentration in the liquid C_l, the velocities u_l, u_g, the pressures p_l, p_g and the temperatures T_l, T_g. As the scaling of the model against parameter ranges expected in nature has shown in Part I, Section 4 [Narbona-Reina et al., 2024], some simplifications are acceptable. We thus neglected the effects of surface tension and heat diffusion within each phase. The gas phase is considered inviscid in its own momentum equation but exerts a viscous drag on the liquid. We also assume a fixed bubble number density, N, and a constant liquid density, ρ_l. This last assumption is common (e.g., [Degruyter et al., 2012, Fowler and Robinson, 2018]) and can be justified by the fact that the liquid density is a weak function of C_l. For instance, the density of a dacitic liquid increases by only $1.3-1.6\%$ for each weight percent of water added [González-Mellado and De la Cruz-Reyna, 2008]. Magma fragmentation is not taken into account as we focus on the dynamics of effusive gas escape. This limits model application to cases where φ is smaller than ~ 0.8 [Melnik and Sparks, 2005].

Under these assumptions, the mass, momentum, and heat balances of our system are:

$$\text{Mass} \quad \begin{cases} \partial_t((1-\varphi)\rho_l) + \operatorname{div}((1-\varphi)\rho_l u_l) = -R^{H_2O} & \text{(2.1a)} \\ \partial_t(\varphi\rho_g) + \operatorname{div}(\varphi\rho_g u_g) = R^{H_2O} & \text{(2.1b)} \\ \partial_t((1-\varphi)\rho_l(1-C_l)) + \operatorname{div}((1-\varphi)\rho_l(1-C_l)u_l) = 0 & \text{(2.1c)} \end{cases}$$

$$\text{Momentum} \begin{cases} \partial_t((1-\varphi)\rho_l u_l) + \operatorname{div}((1-\varphi)\rho_l u_l \otimes u_l) - \operatorname{div}((1-\varphi)\mathcal{D}_l) + \nabla((1-\varphi)p_l) - p_g\nabla(1-\varphi) \\ -K_d\,\varphi(1-\varphi)(u_g-u_l) = (1-\varphi)\rho_l g - \dfrac{u_g+u_l}{2}R^{H_2O} & \text{(2.1d)} \\ \partial_t(\varphi\rho_g u_g) + \operatorname{div}(\varphi\rho_g u_g \otimes u_g) - \operatorname{div}(\varphi\mathcal{D}_g) + \nabla(\varphi p_g) - p_g\nabla\varphi + K_d\,\varphi(1-\varphi)(u_g-u_l) \\ = \varphi\rho_g g + \dfrac{u_g+u_l}{2}R^{H_2O} & \text{(2.1e)} \end{cases}$$

$$\text{Heat} \quad \begin{cases} \partial_t(\varphi c_{pg}\rho_g T_g) + \operatorname{div}(\varphi c_{pg}\rho_g T_g u_g) - \varphi(\partial_t p_g + u_g\cdot\nabla p_g) - \gamma(T_g - T_l) = 0 & \text{(2.1f)} \\ \partial_t((1-\varphi)c_{p_l}\rho_l T_l) + \operatorname{div}((1-\varphi)c_{p_l}\rho_l T_l u_l) - \dfrac{p_l}{\rho_l}R^{H_2O} + \gamma(T_g - T_l) - D_H = 0 & \text{(2.1g)} \end{cases}$$

The viscous stress tensors for the liquid and gas phases are written as

$$\mathcal{D}_l = \eta_l\left(\frac{1}{3}\operatorname{div}u_l\,\mathrm{Id} + 2D(u_l)\right) \qquad D(u_l) = \frac{1}{2}(\nabla u_l + (\nabla u_l)^T) \tag{2.2}$$

$$\mathcal{D}_g = 0. \tag{2.3}$$

The term D_H is the shear heating. Its expression corresponds to u_l times the viscous stress term $\operatorname{div}((1-\varphi)\mathcal{D}_l)$ (see Part I, Section 2.5 [Narbona-Reina et al., 2024]) :

$$D_H = (1-\varphi)\eta_l\left(\frac{1}{3}(\operatorname{div}u_l)^2 + 2D(u_l) : \nabla u_l\right).$$

For this system, the calculated variables are the liquid pressure and the gas density given by, respectively, a simplified version of the Rayleigh-Plesset equation and the ideal gas relationship:

$$p_l = p_g - \frac{1}{\varphi\chi}\left(\operatorname{div}u_l + \frac{R^{H_2O}}{\rho_l(1-\varphi)}\right), \tag{2.4}$$

$$\rho_g = \frac{p_g}{c_0 T_g}, \tag{2.5}$$

where c_0 is the ideal gas constant for water. The gravity vector is $g = (0, 0, \bar{g})$ ($\bar{g} = -9.81\ \mathrm{m/s^2}$) and

$$\chi = \frac{3}{4\eta_l}, \qquad K_d = \frac{\eta_g}{k}, \qquad \rho = \varphi\rho_g + (1-\varphi)\rho_l. \tag{2.6a}$$

where k is the permeability of the magma. Many complexities of how gas bubbles coalesce to yield an interconnected permeable network remain unclear, but a number of constitutive equations relate gas permeability to other geometrical variables of the bubble network. In the original Degruyter model, the permeability, k, entering the drag coefficient, K_d, depends on both φ and the bubble radius, R_b. As a result, K_d depends on the bubble number density, N, because

$$R_b^3 = \frac{3\varphi}{4\pi N(1-\varphi)}.$$

We used instead a permeability relationship valid for effusive eruptions that depends only on φ [Mueller et al., 2005]:

$$k = 10^{-17}(100\varphi)^{3.4}. \tag{2.6b}$$

This choice removes one variable, N, from the inter-model comparison. [Mueller et al., 2005] determined that the exponent in (2.6b) varies between 3 and 3.8; we chose the average value of 3.4 for most runs.

The inter-model comparison focuses on a generic case of andesitic volcano. The liquid viscosity, η_l, is thus that of a rhyolitic melt [Hess and Dingwell, 1996] (see Box 2.1 for a general explanation on empirical relationships):

$$\log_{10}(\eta_l) = -3.545 + 0.833\log_{10}(100C_l) + \frac{9601 - 2368\log_{10}(100C_l)}{T_l - 195.7 - 32.25\log_{10}(100C_l)}, \tag{2.6c}$$

and the exchange term R^{H_2O} is defined following Part I, Section 2.2.2 [Narbona-Reina et al., 2024]:

$$R^{H_2O} = \rho_l \alpha \frac{\varphi^{2/3}(1-\varphi)^{2/3}}{1-\varphi^{1/3}} \quad \text{with} \quad \alpha = 3^{1/3}(4\pi N)^{2/3} D(C_l - k_h\sqrt{p_g}), \tag{2.6d}$$

where D is the diffusion coefficient of water in the silicate liquid and k_h is Henry's constant. In the temperature equations, c_{pg} and c_{pl} are the constant heat capacity of gas and liquid, respectively, and γ is the coefficient of heat transfer between gas and liquid. We chose for γ a parametrization often used in gas–particle systems that depends on the Nusselt number Nu, on the local bubble radius R_b and on the constant heat conductivity of the liquid [Musser and Carney, 2020]:

$$\gamma = \frac{24\kappa_l\varphi\mathrm{Nu}}{R_b^2}, \qquad \mathrm{Nu} = 7 - 10(1-\varphi) + 5(1-\varphi)^2, \qquad R_b^3 = \frac{3\varphi}{4\pi N(1-\varphi)}. \tag{2.6e}$$

The Nusselt number correlation is that of [Gunn, 1978] and it is applicable to gas volume fractions 0–0.65 at small Reynolds number based on the relative velocity $u_g - u_l$.

Box 2.1. On empirical and semi-empirical relationships. Empirical and semi-empirical relationships are frequently used in fluid mechanics and thermodynamics when either the processes are not well understood or when the effects of many parameters are lumped together into fitting coefficients. While empirical relationships have a random accuracy beyond their calibrated range and may not ensure a correct behavior when derived, semi-empirical relationships are often build to recover some physically sound limit behavior. In other words, extrapolating an empirical relationships is hazardous whereas extrapolating a semi-empirical relationships might yields meaningful trends and/or results. Both of these types of relationship excel at performing interpolation between (generally) experimental data points and they are accompanied by an estimate of their accuracy. The fitting coefficients are customarily given with a precision that is commensurate with the level of accuracy of the relationship. In other words, truncating the precision of the coefficients would most commonly cause the relationship to fail in delivering the promised accuracy. Leaving aside the semi-empirical ideal gas law (2.4), we use herein two empirical relationships that govern respectively liquid viscosity and water diffusivity.

Liquid viscosity. As reviewed by [Russell et al., 2022], the simplest temperature dependence shown by silicate liquid viscosity is Arrhenian:

$$\eta_l = A_A + e^{\left(\frac{E_A}{R_A T_l}\right)}$$

where R_A is the universal gas constant, E_A is the activation energy for viscous flow and A_A represents the viscosity at infinite temperature. The parameters A_A and E_A are commonly adjusted to fit the behavior of individual liquid compositions, although the theory suggests that A_A is a constant independent of liquid composition. The Vogel–Fulcher–Tammann (VFT) equation is modification of the Arrhenian relationship that in practice fits better viscosity data:

$$\log_{10}(\eta_l) = A_V + \frac{B_V}{T_l - C_V}$$

where A_V, B_V, C_V are adjustable parameters specific to individual liquids. As before, A_V determines the viscosity at infinite temperature and B_V is a pseudo-activation energy associated with the structural rearrangement of the liquid. The C_V parameter is the temperature at which viscosity becomes infinite. The composition of magmatic liquids is a function of 12 major components ($SiO_2, TiO_2, Al_2O_3, FeO, MnO, MgO, CaO, Na_2O, K_2O, P_2O_5$, F, and H_2O). In our work, C_l is H_2O and $1 - C_l$ represents all the other components. The [Hess and Dingwell, 1996] relationship (2.6c) singles out the H_2O component and thus expands the A_V, B_V, C_V parameters to make the dependence on C_l explicit. One of the most general η_l parametrization is that of [Giordano et al., 2008], which is based on the VFT equation but has lengthy expressions for the 3 fitting parameters that each depends on the 12 major components listed above. Its average misfit is only ± 0.4 log units for a range of liquid composition covering most terrestrial magmas.

Water diffusivity. In Section 3, we use the semi-empirical relationship of [Ni and Zhang, 2008] to describe how D changes as a function of p_g, T_l, and C_l. Once dissolved into a silicate liquid, total water (H_2O_t) dissociates into two species, molecular water (H_2O_m) and hydroxyl (OH). H_2O_m is the dominating diffusing species, and OH is almost immobile. Neglecting OH yields a relationship between the total and molecular diffusivities:

$$D_{H_2O_t} = D_{H_2O_m} \frac{dX_m}{dX_l}$$

where X_m and X_l are the mole fractions of H_2O_t and H_2O_m, respectively. The H_2O_m diffusivity depends exponentially on the H_2O_t content:

$$D_{H_2O_m} = D_0 e^{A_D X_l}$$

where D_0 and A_D are parameters depending on temperature and pressure. As $\frac{dX_m}{dX_l}$ has a lengthy expression, [Ni and Zhang, 2008] recast these two equations into a single, simplified fit of $D_{H_2O_t}$, which we call D_{Ni} in Section 3.

2.1 Equivalent equations for numerical resolution

There are three types of terms that would cause difficulties in the numerical implementation of the system (2.1) (see Part I, Section 2 [Narbona-Reina et al., 2024]): The first type of term is the presence of p_l in (2.4) which is given through a dilatancy like constraint, the second is the presence of both $\partial_t p_g$ and $\partial_t T_g$ in (2.1f), and the third is the temperature coupling through the heat exchange factor γ in (2.1f)-(2.1g).

Both the liquid momentum equation (2.1d) and the dilatancy relationship (2.4) relate the velocity u_l to the two pressures in the system, p_l and p_g. These three variables are thus strongly coupled. By replacing the expression for p_l from (2.4) into (2.1d), we simplify the system, resulting in only u_l and p_g appearing in the momentum equation. As a result of this partial decoupling, p_l becomes an explicitly given variable that is determined by the dilatancy relationship in terms of the other unknowns. We use the expression of the liquid pressure in (2.4) and the definition above $\chi = \frac{3}{4\eta_l}$ to write

$$(1-\varphi)p_l \mathrm{Id} = \left((1-\varphi)p_g - \frac{R^{H_2O}}{\rho_l \varphi \chi}\right)\mathrm{Id} - \frac{4(1-\varphi)\eta_l}{3\varphi}\mathrm{div}u_l\ \mathrm{Id} \tag{2.7}$$

We inject this expression in the momentum equation (2.1d) related to u_l, which yields:

$$\begin{aligned}\partial_t((1-\varphi)\rho_l u_l) + \mathrm{div}((1-\varphi)\rho_l u_l \otimes u_l) - \mathrm{div}\left(\left(\frac{R^{H_2O}}{\rho_l\varphi\chi} + \frac{4(1-\varphi)\eta_l}{3\varphi}\mathrm{div}u_l\right)\mathrm{Id} + (1-\varphi)\mathcal{D}_l\right)\\ + (1-\varphi)\nabla p_g - K_d\,\varphi(1-\varphi)(u_g-u_l) = (1-\varphi)\rho_l g - \frac{u_g+u_l}{2}R^{H_2O}.\end{aligned} \tag{2.8}$$

This equation has the advantage that p_l is not longer present in it but that it satisfies the condition on p_l set by (2.4). This substitution has introduced a dissipative term for the velocity in (2.8), which contributes to the numerical stability of the equation.

We addressed the last two types of potential numerical instability with the same goal of writing a simpler system to solve. The presence of two time derivatives in the same equation makes the stability conditions related to the time step size more difficult to manage (we used a variable-order, variable-step-size backward differentiation formula, BDF, Appendix A.2). This simplification is quite straightforward because both quantities, T_g and p_g, are related by the ideal gas law. Finally, the term $\gamma(T_g - T_l)$ may create numerical issues if the magnitudes of the terms in the equation differ significantly, requiring greater precision in the calculation. The coefficient γ takes values on the order of 10^{10}, so when the other terms in the equation are smaller (D_H and $c_{pl}(1-\varphi)\rho_l\partial_t T_l$ typically span $10^1 - 10^5$ and $10^2 - 10^3$, respectively), this relationship becomes a relaxation equation for $\gamma(T_g - T_l)$, resulting in $T_l \sim T_g$. Eliminating the exchange term from one of the temperature equations has thus the dual advantage of minimizing rounding errors on that equation and of easing the derivation of a single temperature system (see Section 2.2).

Another set of equivalent equations to replace (2.1f)-(2.1g) can be obtained in terms of ρ_g, p_g, T_g from (2.1f) when using (2.1a) and the gas law (2.5). First we write

$$\begin{aligned}\partial_t(\varphi c_0 \rho_g T_g) + \mathrm{div}(\varphi c_0 \rho_g T_g u_g) - \varphi(\partial_t p_g + u_g\cdot\nabla p_g) &= \partial_t(\varphi p_g) + \mathrm{div}(\varphi p_g u_g) - \varphi(\partial_t p_g + u_g\cdot\nabla p_g)\\ &= p_g(\partial_t\varphi + \mathrm{div}(\varphi u_g))\\ &= -p_g\partial_t(1-\varphi) + p_g\mathrm{div}(\varphi u_g)\\ &= \frac{p_g}{\rho_l}R^{H_2O} + p_g\mathrm{div}(\varphi u_g + (1-\varphi)u_l).\end{aligned} \tag{2.9}$$

Thus,

$$c_0\left(\partial_t(\varphi\rho_g T_g) + \mathrm{div}(\varphi\rho_g T_g u_g)\right) - \frac{p_g}{\rho_l}R^{H_2O} - p_g\mathrm{div}(\varphi u_g + (1-\varphi)u_l) = \varphi(\partial_t p_g + u_g\cdot\nabla p_g). \tag{2.10}$$

Equation (2.10) provides a decomposition of the term $\varphi(\partial_t p_g + u_g \cdot \nabla p_g)$, which causes temperature changes due to gas expansion/contraction. This decomposition will yield an alternative equation for the gas temperature that is more amenable to numerical resolution because it will contain only one time derivative on T_g. The inconvenience is that the expansion/contraction has a clear physical meaning, which is not the case of individual terms of the decomposition (e.g., $p_g \mathrm{div}(\varphi u_g + (1-\varphi)u_l)$). Embedding the left-hand-side terms of (2.10) in (2.1f) yields an alternate T_g equation with the time derivative of a single variable (using the definition of heat capacity at constant volume $c_{vg} = c_{pg} - c_0$ for conciseness):

$$c_{vg}\varphi\rho_g(\partial_t T_g + u_g \cdot \nabla T_g) + p_g \mathrm{div}\Big(\varphi u_g + (1-\varphi)u_l\Big) = \gamma(T_g - T_l) - \frac{p_g}{\rho_l} R^{H_2O} - c_{vg} T_g R^{H_2O}. \tag{2.11}$$

As the scaling performed in Part I, Section 4 [Narbona-Reina et al., 2024], suggests, both phases are expected to have similar temperatures. We thus use a formulation that is amenable to suppress one equation if the assumption $T_g = T_l$ is made. The summation of (2.11) and (2.1g) with the value of p_l in (2.4) yields in non-conservative form:

$$\begin{aligned} &c_{vg}\varphi\rho_g\Big(\partial_t T_g + u_g \cdot \nabla T_g\Big) + c_{pl}(1-\varphi)\rho_l\left(\partial_t T_l + u_l \cdot \nabla T_l\right) + p_g \mathrm{div}(\varphi u_g + (1-\varphi)u_l) + (c_{vg}T_g - c_{pl}T_l)R^{H_2O} \\ &= -\frac{R^{H_2O}}{\rho_l \varphi \chi}\left(\mathrm{div} u_l + \frac{R^{H_2O}}{\rho_l(1-\varphi)}\right) + D_H. \end{aligned} \tag{2.12}$$

The favorable characteristic of (2.12) is to avoid the heat exchange term. This equation (2.12) can be used instead of (2.1g) to solve T_l, T_g being solved by (2.11) instead of (2.1f). We have implemented both (2.1f)-(2.1g) and the alternative equations (2.11)-(2.12) and there were no differences in the solutions, nor instabilities caused by the exchange term in the conditions used in the inter-model comparison.

If we assume $T_g = T_l = T$ we write a single equation for T as follows (see eq (5.2e) in Part I [Narbona-Reina et al., 2024]):

$$c_{pm}(\partial_t T + u_T \nabla T) + p_g \mathrm{div}(\varphi u_g + (1-\varphi)u_l) + (c_{vg} - c_{pl})T R^{H_2O} = -\frac{R^{H_2O}}{\rho_l \varphi \chi}\left(\mathrm{div} u_l + \frac{R^{H_2O}}{\rho_l(1-\varphi)}\right) + D_H \tag{2.13}$$

where

$$c_{pm} = \varphi c_{vg}\rho_g + (1-\varphi)c_{pl}\rho_l, \quad u_T = \frac{\varphi c_{vg}\rho_g u_g + (1-\varphi)c_{pl}\rho_l u_l}{c_{pm}}.$$

Note that this equation can also be equivalently deduced from the equivalent equation (2.15) shown below by using (2.9).

2.2 Equivalent equations with physical meaning for $T_g \approx T_l$

All comparisons except that addressing the energy balance were done with a single temperature version of our model to minimize the number of different variables between the two models. This assumption will be shown to be acceptable a posteriori. When both phases have the same temperature, the corresponding equations can be found by first summing (2.1f) and (2.1g):

$$\partial_t(\varphi c_{pg}\rho_g T_g + (1-\varphi)c_{pl}\rho_l T_l) + \mathrm{div}(\varphi c_{pg}\rho_g T_g u_g + (1-\varphi)c_{pl}\rho_l T_l u_l) - \varphi(\partial_t p_g + u_g \cdot \nabla p_g) = \frac{p_l}{\rho_l} R^{H_2O} + D_H, \tag{2.14}$$

and keep one of (2.1f) or (2.1g). For consistency with the system solved numerically (see Section 2.1), we will keep (2.1f). Letting $\gamma \to \infty$ causes (2.1f) to yield $T_g = T_l = T$ (see Part I, Section 5 [Narbona-Reina et al., 2024]). As a result, the summed equation becomes:

$$c_{pn}(\partial_t T + u_n \cdot \nabla T) = \varphi(\partial_t p_g + u_g \cdot \nabla p_g) + \left((c_{pl} - c_{pg})T + \frac{p_l}{\rho_l}\right) R^{H_2O} + D_H \tag{2.15}$$

where

$$c_{pn} = \varphi c_{pg}\rho_g + (1-\varphi)c_{pl}\rho_l, \quad u_n = \frac{\varphi c_{pg}\rho_g u_g + (1-\varphi)c_{pl}\rho_l u_l}{c_{pn}}.$$

3 1.5D transient model

We write the system given by (2.1a), (2.1b), (2.1c), (2.1d), (2.1e), (2.12), (2.4), (2.5), and (2.11) in one dimension for unknowns $\mathcal{U} = \{C_l, \varphi, \rho_g, u_l, u_g, T_l, T_g, p_g, p_l\}$. The independent spatial variable being denoted by z:

$$\partial_t((1-\varphi)\rho_l(1-C_l)) + \partial_z((1-\varphi)\rho_l(1-C_l)u_l) = 0 \tag{3.1a}$$

$$\partial_t((1-\varphi)\rho_l) + \partial_z((1-\varphi)\rho_l u_l) = -R^{H_2O} \tag{3.1b}$$

$$\partial_t(\varphi\rho_g) + \partial_z(\varphi\rho_g u_g) = R^{H_2O} \tag{3.1c}$$

$$\begin{aligned}&\partial_t((1-\varphi)\rho_l u_l) + \partial_z((1-\varphi)\rho_l u_l^2) + \partial_z\left((1-\varphi)p_l\right) + \tilde{\beta}u_l - p_g\partial_z(1-\varphi) - K_d\,\varphi(1-\varphi)(u_g-u_l)\\ &= (1-\varphi)\rho_l g - \frac{u_g+u_l}{2}R^{H_2O}\end{aligned} \tag{3.1d}$$

$$\partial_t(\varphi\rho_g u_g) + \partial_z(\varphi\rho_g u_g^2) + \partial_z(\varphi p_g) - p_g\partial_z\varphi + K_d\,\varphi(1-\varphi)(u_g-u_l) = \varphi\rho_g g + \frac{u_g+u_l}{2}R^{H_2O} \tag{3.1e}$$

$$\begin{aligned}&c_{vg}\varphi\rho_g\left(\partial_t T_g + u_g\partial_z T_g\right) + c_{pl}(1-\varphi)\rho_l\left(\partial_t T_l + u_l\partial_z T_l\right) + p_g\partial_z(\varphi u_g + (1-\varphi)u_l) + (c_{vg}T_g - c_{pl}T_l)R^{H_2O}\\ &= -\frac{R^{H_2O}}{\rho_l\varphi\chi}\left(\partial_z u_l + \frac{R^{H_2O}}{\rho_l(1-\varphi)}\right) + D_H\end{aligned} \tag{3.1f}$$

$$c_{vg}\varphi\rho_g(\partial_t T_g + u_g\partial_z T_g) + p_g\partial_z\Big(\varphi u_g + (1-\varphi)u_l\Big) + \Big(\frac{p_g}{\rho_l} + c_{vg}T_g\Big)R^{H_2O} = \gamma(T_g - T_l) \tag{3.1g}$$

$$p_g = c_0\rho_g T_g \tag{3.1h}$$

$$p_l = p_g - \frac{1}{\varphi\chi}\left(\partial_z u_l + \frac{R^{H_2O}}{\rho_l(1-\varphi)}\right) \tag{3.1i}$$

The term $\tilde{\beta}u_l$ in (3.1d) stems from the 1.5D assumption that a volcanic conduit can be represented by a cylinder. To keep the effect of viscous friction against the cylinder walls despite the 1D approximation, the common approach is to replace the viscous terms of the momentum equations by a boundary layer approximation, which yields a 1.5D formulation. This approximation can be done several ways and this choice affects the 1.5D formulation of the viscous heating, D_H. The most straightforward dimension reduction is a first-order discretization over the conduit radius r_c (see (2.2)), which yields:

$$\mathrm{div}((1-\varphi)\mathcal{D}_l) \approx \frac{1-\varphi}{4}\tilde{\beta}u_l + \partial_z\left((1-\varphi)\frac{\eta_l}{3}\partial_z u_l\right) \qquad \text{with} \qquad \tilde{\beta} = \frac{8\eta_l}{r_c^2}. \tag{3.2}$$

The corresponding viscous heating in the liquid temperature equation is:

$$D_H = (1-\varphi)\left(\frac{1}{4}\tilde{\beta}u_l^2 + \frac{\eta_l}{3}\left(\partial_z u_l\right)^2\right). \tag{3.3}$$

Another dimension reduction approach was used in the Degruyter model. When $\varphi \to 0$, the isothermal system (2.1) yields a classic incompressible, single phase Navier-Stokes equation. Under the assumption of steady, parallel, axisymmetric flow in a cylinder, the solution of that single phase system yields [Schlichting and Gersten, 2017]:

$$\mathrm{div}((1-\varphi)\mathcal{D}_l) \approx \tilde{\beta} u_l. \tag{3.4}$$

There is no term containing the second viscosity coefficient because of the assumption of incompressibility. The corresponding viscous heating in the liquid temperature equation is thus:

$$D_H = \tilde{\beta} u_l^2. \tag{3.5}$$

To minimize the cases studies in the model comparison, we only considered this second method of 1.5D approximation by using (3.4) in the momentum equation and (3.5) in the temperature equation but we evaluated the impact of considering the viscous heating (3.3) that includes the second viscosity term.

Water diffusion, D, present in the expression of R^{H_2O} (2.6d), was constant in many comparison runs, but a variable case was also considered. It uses the model of [Ni and Zhang, 2008] (see Box 2.1 for a general explanation on empirical relationships):

$$\ln\left(\frac{D_{\mathrm{Ni}}}{X_l}\right) = 13.47 - 50X_l + 7.1\sqrt{X_l} + 1.89\times10^{-9}p_g - \frac{1}{T_l}(9532 - 91933X_l + 13403\sqrt{X_l} + 3626\times10^{-9}p_g) \tag{3.6}$$

where p_g has been used to estimate ambient pressure instead of p_l to avoid creating a dependency between p_l and R^{H_2O}. This approximation has a lesser effect than the uncertainty on D_{Ni} (a factor 1.6, [Ni and Zhang, 2008]) because $|p_g - p_l| < 1$ MPa in all runs. The molar fraction of dissolved water, X_l, is given by:

$$X_l = \frac{1}{1 + \frac{M_{H_2O}Y_l}{C_l}} \tag{3.7}$$

where $M_{H_2O} = 0.018$ kg/mol is the molar mass of water and $Y_l = 15.4$ mol/kg is a representative value of the sum of molar fractions of the major oxides composing a rhyolitic liquid.
Finally, the total energy balance of the system (3.1) is dissipative if:

$$\begin{aligned}
&\partial_t\left((1-\varphi)\rho_l\frac{|u_l|^2}{2} + \varphi\rho_g\frac{|u_g|^2}{2} + g((1-\varphi)\rho_l + \varphi\rho_g) + \varphi c_{vg}\rho_g T_g + (1-\varphi)c_{p_l}\rho_l T_l\right)\\
&+\partial_z\left((1-\varphi)\rho_l u_l\frac{|u_l|^2}{2} + \varphi\rho_g u_g\frac{|u_g|^2}{2} + g((1-\varphi)\rho_l u_l + \varphi\rho_g u_g) + (1-\varphi)p_l u_l + \varphi c_{pg}\rho_g T_g u_g + (1-\varphi)c_{p_l}\rho_l u_l T_l\right)\\
&\leq\\
&-K_d\varphi(1-\varphi)|u_g - u_l|^2 - \varphi(1-\varphi)\chi(p_g - p_l)^2
\end{aligned} \tag{3.8}$$

Remark 3.1. *All the terms in the time derivative are positive and the terms on the right-hand side of the inequality are negative.*

4 The Degruyter model

The Degruyter system [Kozono and Koyaguchi, 2009,Degruyter et al., 2012] is a 1.5D, steady-state, two-fluid model with a constant temperature, T, one pressure, p, no momentum exchange terms due to phase change, and no conservation equation for water. Its unknowns are u_g, u_l, p, ρ_g, and φ:

$$\partial_z((1-\varphi)\rho_l u_l) = -R^{De} \tag{4.1a}$$

$$\partial_z(\varphi\rho_g u_g) = R^{De} \tag{4.1b}$$

$$(1-\varphi)\rho_l u_l \partial_z u_l + (1-\varphi)\partial_z p + \tilde{\beta} u_l - K_d\,\varphi(1-\varphi)(u_g - u_l) = (1-\varphi)\rho_l g \tag{4.1c}$$

$$\varphi\rho_g u_g \partial_z u_g + \varphi\partial_z p + K_d\,\varphi(1-\varphi)(u_g - u_l) = \varphi\rho_g g \tag{4.1d}$$

$$p = c_0 \rho_g T \tag{4.1e}$$

To reduce the number of free parameters of the inter-model comparison, we choose the permeability relationship (2.6b) because it only depends on φ.

The mass exchange term R^{De} differs from R^{H_2O}:

$$R^{De} = q\partial_z n, \tag{4.2}$$

where q is the constant mass flux ($\mathrm{kg\ s^{-1}m^{-2}}$) and n is the ratio between the mass exsolved water and the total mass:

$$n = \frac{C_c - k_h\sqrt{p}}{1 - k_h\sqrt{p}} \tag{4.3}$$

where C_c is the initial constant amount of water. The formulation (4.2) has two underlying assumptions. First, the amount of dissolved water is assumed to be at saturation at all times. This is a consequence of considering only one pressure in the system. The second assumption is that C_c is constant and equal to the value at the bottom boundary. These two assumptions constrain the water mass balance to be in a closed system, which is at odds with the mass conservation (4.1a)-(4.1b) when $u_l \neq u_g$. This inconsistency has far reaching consequences on the steady-state solutions of the system (4.1), complicating the comparison with our 1.5D model.

We assume here that the liquid density is constant and thus independent from the amount of dissolved water. To implement a visual illustration of how water mass is treated by each model, we express n, C_l, and C_c in terms of masses:

$$n = \frac{M_i - M_d(z)}{M_i + M_l}, \qquad C_l = \frac{M_d(z)}{M_d(z) + M_l}, \qquad C_c = \frac{M_i}{M_i + M_l} \tag{4.4}$$

where M_i is the total mass water at the bottom of the conduit, M_d is the mass of water dissolved in the melt, and M_l is the constant mass of liquid. For clarity, we explicitly write the dependency of the masses on z where appropriate. We define C_l^{eq} as the amount of dissolved water at saturation,

$$C_l^{\mathrm{eq}} = k_h\sqrt{p_g}. \tag{4.5}$$

The total amount of water at any given location is given by the variable C_T (see equation (2.53) in Part I [Narbona-Reina et al., 2024]), which also can be expressed in terms of masses:

$$C_T = \frac{\varphi\rho_g + (1-\varphi)\rho_l C_l}{\rho} = \frac{\varphi\rho_g V + (1-\varphi)\rho_l C_l V}{\varphi\rho_g V + (1-\varphi)\rho_l C_l V + (1-\varphi)\rho_l(1-C_l)V} = \frac{M_e(z) + M_d(z)}{M_e(z) + M_d(z) + M_l} \tag{4.6}$$

where V is a small volume at position z and M_e is the mass of exsolved water (i.e. the mass of gas). This definition of C_T yields the useful relationship $(1-\varphi)\rho_l(1-C_l) = \rho(1-C_T)$ that can be used in (3.1a) with the total mass conservation (3.1b)+(3.1c) to obtain:

$$\partial_t C_T + u_l \partial_z C_T = \frac{1-C_T}{\rho}\partial_z(\varphi\rho_g(u_l-u_g)). \tag{4.7}$$

C_T is thus a transported amount of water that is unaffected by exsolution but that is subject to gain and losses when there is gas-liquid separation (i.e. $u_g \neq u_l$).

Remark 4.1. *A perhaps more intuitive way to define C_T is to use the mass fraction of gas, W_g:*

$$\frac{1}{W_g} = 1 + \frac{\rho_l(1-\varphi)}{\rho_g\varphi},$$

which yields $C_T = W_g + (1-W_g)C_l$.

At the bottom of the conduit, $z=0$, $M_e + M_d = M_i$ and so $C_c = (C_T)_{|z=0}$. When liquid and gas have different velocities, C_T is not constant. We can thus define a new ratio between the mass of exsolved water and the total mass, $n^{\mathrm{eq}}(z)$, that is based on $C_T(z)$ and, in order to compare with the Degruyter model, that assumes $C_l = C_l^{\mathrm{eq}}(z)$:

$$n^{\mathrm{eq}} = \frac{C_T(z) - C_l^{\mathrm{eq}}}{1 - C_l^{\mathrm{eq}}}.$$

Using (4.6), it becomes

$$n^{\mathrm{eq}} = \frac{\varphi\rho_g}{\varphi\rho_g + (1-\varphi)\rho_l}. \tag{4.8}$$

We will plot in the model solutions the initial water content C_c, the total water content, C_T, and both ratios between exsolved water and total mass, n (4.3) and n^{eq} (4.8). That water mass conservation is not maintained is apparent when $C_c \neq C_T$ and $n \neq n^{\mathrm{eq}}$. Finally, we define the equilibrium degassing porosity by using the relationship between C_T and φ:

$$\varphi^{\mathrm{eq}} = \left(1 + \frac{\rho_g(C_T-1)}{\rho_l(C_l^{\mathrm{eq}} - C_T)}\right)^{-1}. \tag{4.9}$$

Note that φ^{eq} has traditionally been defined by assuming a single pressure and considering $(C_T)_{|z=0} = C_c$ known [Jaupart and Allègre, 1991]. This is germane for the Degruyter model. When comparing with our transient model, however, the value given by (4.9) implies $\partial_t\varphi = 0$ only if $p_l = p_g$ as well because (4.9) only involves p_g through ρ_g and C_l^{eq}.

Finally, the energy equation of the Degruyter model is dissipative if:

$$\begin{aligned}
&\partial_z\left(\varphi\rho_g u_g\frac{u_g^2}{2} + (1-\varphi)\rho_l u_l\frac{u_l^2}{2} + g(\varphi\rho_g u_g + (1-\varphi)\rho_l u_l) + p((1-\varphi)u_l + \varphi u_g)\right)\\
&\leq\\
&\quad -\frac{u_l^2-u_g^2}{2}R^{De} - \tilde{\beta}u_l^2 - K_d\varphi(1-\varphi)(u_g-u_l)^2 - \left(\frac{1}{\rho_l} - \frac{1}{\rho_g}\right)pR^{De} - \varphi u_g\partial_z p.
\end{aligned} \tag{4.10}$$

The sum of all right-hand side terms has to be negative to ensure a dissipative energy balance. Taken individually, only the second and third terms are always negative. The right-hand side has thus no predefined sign and dissipation is not guaranteed.

5 Numerical resolution

In this section numerical approximation and computational techniques are specified in order to be able to reproduce the results presented in this work. To solve the transient model we use the *Comsol Multiphysics v5.6* software. Appendix A contains the implementation details of the 1.5D system (3.1) in non conservative form.

The flow in the volcano conduit is considered as a quasi 1D flow along the depth of the conduit. Thus, the domain is just defined by $\Omega = [0, H]$ for H being the conduit length. We introduce the notation for the inlet boundary, at the base of the domain, $\Gamma_{\text{in}} : z = 0$ and the outlet boundary, at the top of the domain, $\Gamma_{\text{out}} : z = H$. Obviously for this configuration there is no wall boundary.

5.1 Initial conditions

Initial values must be prescribed for the system (3.1); we will use the superscript i in variables to denote them. The initial guess on the distribution p_g^i is linear and corresponds to the pressure gradient of a bubble-free magma:

$$p_g^i = p_{\text{top}} - \rho_l g(H - z) \tag{5.1}$$

where p_{top} is the fixed pressure at the top boundary of the conduit.

There are different ways to choose the initial value for φ^i. Ideally, φ can be initialized with a steady-state profile, such as the output of the Degruyter model. Here, to avoid circular reasoning, we specify the initial φ distribution as a linear function of depth:

$$\varphi^i = \varphi_0 \frac{z}{H} + \varphi_1, \tag{5.2}$$

where φ_0 and φ_1 are constants.

These initial guesses of p_g^i and φ^i must be compatible with each other and with the algebraic equations in (3.1). To minimize incompatibility, we use the same approach as in the analysis of the relaxed system in Part I, Section 5 [Narbona-Reina et al., 2024], by canceling mass exchange ($R^{H_2O} = 0$) and pressure difference (3.1i). Together with (3.1h), these assumptions yield:

$$C_l^i = k_h \sqrt{p_g^i}, \qquad p_l^i = p_g^i, \qquad \rho_g^i = \frac{p_g^i}{c_0 T^i}, \tag{5.3}$$

with T^i a fixed constant temperature T_{in},

$$T^i = T_{\text{in}}. \tag{5.4}$$

When two temperatures are considered, $T_g^i = T_l^i = T^i$. Finally, $u_l^i = u_g^i = u^i$ to minimize the coupling of the momentum equations by drag. Hence,

$$\begin{aligned} &(C_l)_{|t=0} = C_l^i; \qquad (\varphi)_{|t=0} = \varphi^i; \qquad (u_l)_{|t=0} = (u_g)_{|t=0} = u^i; \qquad (T_l)_{|t=0} = (T_g)_{|t=0} = T_{\text{in}}; \\ &(\rho_g)_{|t=0} = \rho_g^i; \qquad (p_l)_{|t=0} = (p_g)_{|t=0} = p_g^i, \end{aligned} \tag{5.5}$$

All computational values will be specified later in Table 2.

5.2 Boundary conditions

The 1.5D model presented here does not include thermal conductivity. Also, the viscous part of the gas stress tensor, $\mathcal{D}_g$, is neglected (see equation (2.3)) and the liquid viscosity tensor, $\mathcal{D}_l$, is replaced by the damping term $\tilde{\beta} u_l$ (see equation (3.4)). So even if there is a viscous component in the equation (3.1d) coming from the liquid pressure term through (3.1i) (see also (A.3d) in Appendix A):

$$\partial_z((1-\varphi)p_l) = \partial_z \left((1-\varphi)p_g - \frac{4\eta_l}{3\varphi} \frac{R^{H_2O}}{\rho_l} - \frac{4\eta_l(1-\varphi)}{3\varphi} \partial_z u_l \right), \tag{5.6}$$

following the analysis in Part I, Section 3 [Narbona-Reina et al., 2024], boundary conditions must be imposed in the same fashion as if the system were inviscid.

For the one-dimensional case, at the inflow boundary there must be five conditions (two for gas, three for liquid) with one additional condition on φ if it is not already considered for the liquid. At the outflow boundary, two conditions (one for gas, one for liquid) must be set (see Table 5 in Part I, Section 3 [Narbona-Reina et al., 2024]). We consider the options specified in equation (3.12) in Part I [Narbona-Reina et al., 2024] for this type of systems that we remind here:

- For the inlet boundary, two options are considered by imposing the velocity (BCU) or the pressure (BCP) value. For both of them, fixed values of the concentration C_l and the volume fraction φ must be imposed. For BCU type, velocities must be given such that $u_l > 0, u_g > 0$ and we have to prescribe the value of the liquid temperature and to choose between the density ρ_g or the temperature T_g for the gas phase. For BCP type, pressures and temperatures are imposed for the two phases.
- For the outlet boundary, only the pressures have to be defined.

In the case of BCP, notice that the pressure values must be set to ensure that the flux enters the domain at the inlet boundary and there is no reflection at the outlet boundary. The specific values of the parameters introduced in this section are in Table 2.

5.2.1 Boundary conditions at the inlet ($\Gamma_{\text{in}} : z = 0$)

In the application developed here we use BCP type to impose an inflow condition at the inlet. We must prescribe values for the pressures p_g and p_l and the temperatures T_l and T_g together with the concentration C_l and volume fraction φ. It is important to remark that we implemented the numerical solution by keeping conservative variables for equations (3.1a), (3.1b) and (3.1c) (Appendix A). So, instead of C_l, we must prescribe $\rho_l(1-\varphi)(1-C_l)$. Similarly, $\varphi\rho_g$ and $\rho_l(1-\varphi)$ will be prescribed instead of φ and ρ_g individually. Thus, compatibility with the system and the initial conditions must be carefully looked over. The boundary conditions read:

$$\begin{gathered}(p_l)_{|\Gamma_{\text{in}}} = (p_g)_{|\Gamma_{\text{in}}} = p_{\text{in}}; \quad (T_l)_{|\Gamma_{\text{in}}} = (T_g)_{|\Gamma_{\text{in}}} = T_{\text{in}}; \quad (\varphi\rho_g)_{|\Gamma_{\text{in}}} = (\varphi_{\text{in}} p_{\text{in}}/(c_0 T_{\text{in}}))_{\text{in}}; \\ (\rho_l(1-\varphi)(1-C_l))_{|\Gamma_{\text{in}}} = (\rho_l(1-\varphi_{\text{in}})(1-(C_l)_{\text{in}})); \quad (\rho_l(1-\varphi))_{|\Gamma_{\text{in}}} = \rho_l(1-\varphi_{\text{in}}),\end{gathered} \tag{5.7}$$

where the following variables have the same values as for the initial conditions: $p_{\text{in}} = p_g^i$, $\varphi_{\text{in}} = \varphi^i$ and $(C_l)_{\text{in}} = C_l^i$. The boundary condition of $\varphi\rho_g$ has been set to ensure compatibility with (3.1h) as in (5.3).

These BCP conditions are more favorable than the BCU type for the inlet because setting $(C_l)_{\text{in}}$ to C_l^{eq} is the only way to ensure that $R^{H_2O} = 0$ if $\varphi > 0$. While this is straightforward for the BCP type, it creates difficulties for BCU because the corresponding equilibrium porosity (4.9) is the porosity such that $C_l = C_l^{eq}$. So both C_l^{eq} and φ^{eq} depends on p_g.

To illustrate why it is not possible to leave p_g unspecified and ensure $R^{H_2O} = 0$ in BCU, let's consider an inflow condition for the two velocities and two specified temperatures (see Part I, Section 3 [Narbona-Reina et al., 2024], for a justification of this starting choice and a wider discussion). As the drag term is a function of φ, setting equal velocities is a natural choice to maximize decoupling between the two momentum equations. As a result, the total water content C_T will be a transported quantity at the boundary (see (4.7)). Thus, setting C_T at the boundary would be a compatible, stable choice. The corresponding, alternate equation solved, however, is the conservation of $\rho_l(1-\varphi)(1-C_l)$ (3.1a), which is equivalent to $\rho(1-C_T)$. While this equation does not depend on any source term, it depends on p_g through the product $(1-\varphi)(1-C_l)$. In addition, the most common choice for gas dynamics system is to impose the gas

density $\varphi\rho_g$, which is a product that also depends on p_g. Eliminating p_g from these products is not feasible algebraically because the three conditions $(1-\varphi)(1-C_l)=C_1$, $\varphi\rho_g=C_2$, and $C_l=k_h\sqrt{p_g}$ (where C_1, C_2 are set constants) yield a third-degree equation on p_g, precluding the option of letting it free. Switching (3.1a) for (4.7) would not alleviate that issue. In other words, BCU implies that $R^{H_2O}\neq 0$, which in our experience can only be stabilized by an additional numerical boundary condition (see below). An additional limitation of letting p_g free is that p_g cannot decrease below the critical value $(C_l^{eq}/k_h)^2$ because then $\varphi^{eq}<0$.

Another advantage of BCP conditions is that if the inlet pressure is a prescribed function of time, such as $p_{\rm in}(t)$, an algorithm preserving $R^{H_2O}=0$ at the inlet at all times can be implemented by calculating $C_T(t_0)$ at the initial time t_0 using (4.6) with $\varphi_{\rm in}(t_0)$. Then, as $t>t_0$, ρ_g is updated with $p_{\rm in}(t)$ and (3.1h), $(C_l)_{\rm in}$ is updated with (4.5), and $\varphi_{\rm in}$ is updated using (4.9). Finally, the conservative variables are updated according to (5.7). This implementation can be used to couple the volcanic conduit flow to a deeper reservoir source (e.g., [Melnik and Sparks, 2005, Kozono and Koyaguchi, 2012]).

5.2.2 Boundary conditions at the outlet boundary ($\Gamma_{\rm out}: z=H$)

To avoid nonphysical results when $p_{\rm top}$ is atmospheric (see Section 6.1.3) and thus ensure a realistic model intercomparison, we imposed pressure equality in most runs by using:

$$(p_g)_{|\Gamma_{\rm out}}=(p_l)_{|\Gamma_{\rm out}}=p_{\rm top}. \tag{5.8a}$$

A more accurate outflow boundary condition is to consider that the gas phase equilibrates with the atmosphere while p_l follows the dilation relationship (3.1i):

$$(p_g)_{|\Gamma_{\rm out}}=p_{\rm top},\qquad (p_l)_{|\Gamma_{\rm out}}=p_{\rm top}-\left(\frac{4\eta_l}{3\varphi(1-\varphi)}\right)_{|\Gamma_{\rm out}}\left(\Big((1-\varphi)\partial_z u_l\Big)_{|\Gamma_{\rm out}}+\frac{1}{\rho_l}(R^{H_2O})_{|\Gamma_{\rm out}}\right) \tag{5.8b}$$

with

$$\frac{1}{\rho_l}(R^{H_2O})_{|\Gamma_{\rm out}}=3^{1/3}\Big(4\pi N\varphi(1-\varphi)\Big)^{2/3}_{|\Gamma_{\rm out}}D\frac{(C_l)_{|\Gamma_{\rm out}}-k_h\sqrt{p_{\rm top}}}{1-(\varphi)^{1/3}_{|\Gamma_{\rm out}}}.$$

Finally, a third possible outflow boundary condition is to consider the mixture momentum equation (see Part I, Section 4 [Narbona-Reina et al., 2024]) and impose an average pressure:

$$(\varphi p_g+(1-\varphi)p_l)_{|\Gamma_{\rm out}}=p_{\rm top} \tag{5.8c}$$

Thanks to (3.1i), this condition reads

$$(p_g)_{|\Gamma_{\rm out}}=p_{\rm top}+\left(\frac{1-\varphi}{\varphi\chi}\right)_{|\Gamma_{\rm out}}\left(\mathrm{div}u_l+\frac{R^{H_2O}}{\rho_l(1-\varphi)}\right)_{|\Gamma_{\rm out}}$$

and

$$(p_l)_{|\Gamma_{\rm out}}=p_{\rm top}-\left(\frac{1}{\chi}\right)_{|\Gamma_{\rm out}}\left(\mathrm{div}u_l+\frac{R^{H_2O}}{\rho_l(1-\varphi)}\right)_{|\Gamma_{\rm out}}$$

In case the velocity is incoming at this boundary, that is $u_l\cdot\vec{n}<0$ or $u_g\cdot\vec{n}<0$, we should impose the values for the other variables. Similarly than before, they are given by

$$\begin{aligned}(T_l)_{|\Gamma_{\rm out}}=T^i,\quad (\rho_l(1-\varphi)(1-C_l))_{|\Gamma_{\rm out}}&=\rho_l(1-\varphi^i)(1-k_h\sqrt{p_{\rm top}}),\\ (\rho_l(1-\varphi))_{|\Gamma_{\rm out}}&=\rho_l(1-\varphi^i)\qquad \text{IFF}\qquad u_l\cdot\vec{n}<0\\ (T_g)_{|\Gamma_{\rm out}}=T^i,\qquad (\varphi\rho_g)_{|\Gamma_{\rm out}}&=\tfrac{\varphi^i p_{\rm top}}{c_0T^i}\quad \text{IFF}\qquad u_g\cdot\vec{n}<0\end{aligned}\ . \tag{5.8d}$$

This case never occurred in the performed numerical simulations even though it was implemented.

5.2.3 Additional numerical boundary conditions

As discussed in the literature [Rudy and Strikwerda, 1981, Poinsot and Lele, 1992, Choudhary et al., 2016], the physical and mathematical boundary conditions are not always enough to solve the problem numerically and additional numerical (also called "soft") boundary conditions may be considered. For example, [Poinsot and Lele, 1992] considered the case of imposing both velocity and temperature at the inlet, and found that an additional numerical condition on the density must be added to keep compatibility with its corresponding equation. In most cases, these numerical conditions consist of an extrapolation of the concerned variables at the boundary, that it is interpreted as a zero normal derivative through this boundary (Neumann condition).

The restrictive outlet boundary condition of equal pressures (5.8a) involves numerical boundary conditions because of the peculiar closure expression for the liquid pressure (3.1i). As pointed out at the beginning of this section, the liquid pressure involve an equivalent diffusion term for the liquid velocity ((5.6), see also (A.3d) in Appendix A). For such equation type, we usually have to prescribe a Neumann condition to solve the second derivative of the velocity. In our case, this condition comes from the liquid pressure since considering $p_l = p_g$ at the boundaries means that the diffusive term (5.6) is zero at the boundary:

$$\left(\frac{4\eta_l}{3\varphi}\frac{R^{H_2O}}{\rho_l} + \frac{4\eta_l}{3\varphi}(1-\varphi)\partial_z u_l\right)_{|\Gamma_j} = 0, \quad \text{for any boundary} \quad j = \text{in}, \text{out}. \tag{5.9}$$

This is the additional numerical condition considered at both boundaries to correctly solve the velocity u_l. Notice that simply imposing $\partial_z u_l = 0$ would be incorrect because it yields a wrong liquid pressure value. This condition is not additional boundary conditions needed to close the system but it is needed for algorithmic reasons in the numerical implementation. This condition just duplicates information without over-specifying the problem.

5.3 The Degruyter model

The numerical resolution of the Degruyter model was performed using the *Octave v6.2* software. We refer the reader to [Degruyter et al., 2012] for details on implementation. It is a two-point boundary value system with $p_{|\Gamma_{\text{out}}} = p_{\text{top}}$ and $p_{|\Gamma_{\text{in}}} = p_{\text{in}} = \rho_l g H$. The algorithm does not need initial values for C_l, as the equivalent variable, C_l^{eq}, is given by (4.5). Similarly, only an inlet value of $\varphi_{|\Gamma_{\text{in}}} = \varphi_1$ is needed. The inlet velocities are $(u_l)_{|\Gamma_{\text{in}}} = (u_g)_{|\Gamma_{\text{in}}} = u_{\text{in}}$. The solution is found thanks to a bisection algorithm, so two initial bounding values for u_{in} are chosen so that they yield one positive and one negative residual, respectively. The bounding values are selected manually through the constant mass flow rate q:

$$u_{\text{in}} = q\left(\frac{n_{\text{in}}}{(\rho_g)_{\text{in}}} + \frac{1-n_{\text{in}}}{\rho_l}\right) \quad \text{with} \quad (\rho_g)_{\text{in}} = \frac{c_0 T}{p_{\text{in}}}, \quad n_{\text{in}} = \frac{C_c - C_l^{\text{eq}}}{1 - C_l^{\text{eq}}}, \quad C_c = \frac{\varphi_1(\rho_g)_{\text{in}} + (1-\varphi_1)\rho_l C_l^{\text{eq}}}{\varphi_1(\rho_g)_{\text{in}} + (1-\varphi_1)\rho_l}$$

where T is a constant temperature.

6 Results

Table 2 lists the constant parameters used in the model inter-comparison. These values are typical of an effusive eruption at an andesitic volcano. In addition to these parameters, several constant values for D ($0, 10^{-13}$, and 10^{-8} m^2/s) plus the variable diffusion, D_{Ni}, given by (3.6)-(3.7) were chosen to cover the range typical of rhyolitic liquids and the end-member of no mass exchange. Note that, for water vapor, we used the relationship between the heat capacity c_{pg}

and the constant c_0 given by $c_{pg}/c_0 = 4.4$. All transient runs except one were done by assuming $T_g = T_l$.

When initialized with the values of Table 2 and an initial guest for q, the Degruyter model converges towards a constant mass flow rate of 5.3×10^5 kg/s, which corresponds to an inlet velocity of 0.3 m/s. Such an ascent rate corresponds to effusive conditions near the transition between effusive and explosive behavior [Cassidy et al., 2018]. These conditions are consistent with the fact that, near the top boundary (surface), φ nearly reaches 0.8 before decreasing of a few percent when reaching the surface. These conditions, close to magma fragmentation, allowed us to maximize the range of φ values explored in this comparison. We used the steady-state solution of the Degruyter model to obtain the spatial distribution of φ. We then approximated that distribution by adjusting φ_0 in (5.2) to obtain the reference initial condition for the transient model. The steady states reached by the transient model will be shown to be independent of φ_0.

Parameter	Value	Definition (unit)
H	5000	conduit height (m)
$\bar{g}$	-9.81	gravity acceleration (m/s^2)
ρ_l	2450	liquid density (kg/m^3)
η_g	2×10^{-5}	gas viscosity (Pa s)
c_0	461.4	gas constant for water (J/kg K)
k_h	4.11×10^{-6}	solubility coefficient (Pa$^{-1/2}$)
r_c	15	conduit radius (m)
u^i	0	initial speed (m/s)
T_{in}, T	1138	(inlet) temperature (K)
p_{top}	0.1	outlet pressure (MPa)
p_{in}	120	inlet pressure (MPa)
φ_1	5×10^{-3}	inlet porosity

(a) Parameters common to both models

Parameter	Value	Definition (unit)
D	$0 - 10^{-8}$	melt water diffusion (m$^2/s$)
N	10^{12}	bubble number density (m^{-3})
c_{pl}	1000	liquid heat capacity (J/kg K)
c_{pg}	2030	gas heat capacity (J/kg K)
κ_l	2.3	liquid heat conductivity (W/m K)
φ_0	$0.1 - 0.7$	outlet porosity minus φ_1

(b) Parameters only present in the transient model

Table 2: Constant parameters used in the inter-model comparison. In addition, D varies according to (3.6) in some transient runs.

6.1 Steady state

6.1.1 Constant temperature

For clarity, system (2.1) is referred to as the transient model and system (4.1) is referred to as the Degruyter model. All steady-state solutions of the transient model were obtained with the *COMSOL Multiphysics* stationary solver that ignored all the time derivatives of the equation system. The solver was initialized by transient solutions that will be described in Section 6.2.

The value of D significantly changes the steady state reached by the transient model. Figure 1A shows steady-state profiles of gas volume fraction (φ, here referred to as porosity) for progressively vanishing values of D plus the variable case with D_{Ni}. At $D = 0$ m^2/s, which suppresses mass exchange by setting $R^{H_2O} = 0$, the steady-state porosity evolution is only due to gas expansion and permeable flow. As a result, porosity remains low from depth to 4.5 km, after which it increases sharply to reach ~ 90 vol% at the surface. The water dissolved in the melt, C_l, is constant because it is imposed at the base of the conduit and that boundary value is advected to the top without mass exchange. The range of values covered by D_{Ni} from the base to the top of the conduit is $10^{-11} - 10^{-12}$ m^2/s, respectively. So when $D \geq 10^{-12}$ m^2/s, the steady-state porosity profiles from the transient model are close to that of the Degruyter

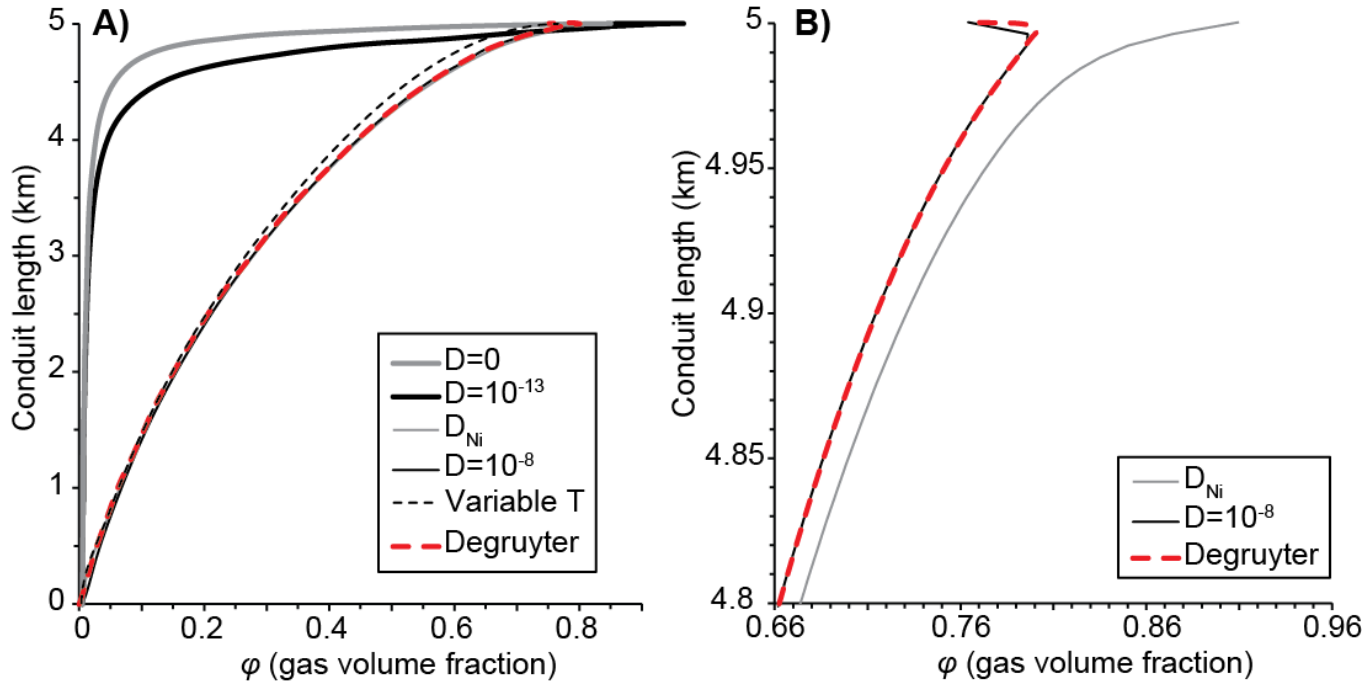

Figure 1: Gas volume fraction (φ) as a function of height in the conduit for the Degruyter run and for the transient model at steady state with several values of diffusion (isothermal) and D_{Ni} (variable, single temperature). A) Full conduit length (curves for $D = 10^{-8}, D_{\mathrm{Ni}}$, and Degruyter almost overlap). B) Closeup of the 200 last meters of the conduit before the surface.

model. When focusing on the shallowest part of the conduit (Figure 1B), only the case with $D = 10^{-8}$ m^2/s reproduces the porosity reduction near the surface of the Degruyter model. Such a diffusion value is unrealistically high for natural melts [Ni and Zhang, 2008], suggesting that perfect equilibrium degassing during the whole ascent is unattainable.

The shallow porosity reduction in the Degruyter model is due to permeable flow that induces $u_g > u_l$ and gas evacuation [Degruyter et al., 2012]. This gas/liquid separation is affected by mass transfer, which is driven by the assumption of equilibrium degassing. In the Degruyter model, equilibrium degassing is enforced by the dual condition of pressure equilibrium, $p_g = p_l$, and no water supersaturation, $C_l = C_l^{\mathrm{eq}}$. In the transient model, the first condition is nearly fulfilled regardless of the diffusion value because the gas overpressure with respect to the liquid pressure $(p_g - p_l)$ is small everywhere except near the surface, where it remains smaller than 0.003 MPa (Figure 2A). There is a thin boundary layer in the distribution of the gas overpressure near the outlet. It caused by the assumption that both outlet pressures are equal to atmospheric, and Section 6.1.3 presents the consequences of relaxing this assumption.

How well the transient model solution fulfills the second condition, water supersaturation (i.e. $C_l \neq C_l^{\mathrm{eq}}$), can be measured two ways. One measure is the difference $C_l - C_l^{\mathrm{eq}}$ (Figure 2B). The other is the difference between the saturation pressure $(C_l/k_h)^2$ and p_g because this measure of supersaturation can be directly related to the likelihood of a (new) nucleation event (Figure 2C). Bubble nucleation is a dynamic process but it is often simplified in the case of heterogeneous nucleation (i.e. bubble nucleation on pre-existing crystals) by setting a threshold in pressure drop (>5 MPa for oxides, >30 MPa for biotite; [Hurwitz and Navon, 1994]; [Gardner and Denis, 2004]) above which the rate of nucleation is large enough to modify N significantly over the time period of interest.

Both measures yield similar trends, so we only focus on the supersaturation pressure for the different values of dif-

fusion (Figure 2C). The case with D_{Ni} has a supersaturation pressure ~ 1 MPa over most of the conduit and between 1 and 5 MPa at both conduit ends, possibly triggering a second nucleation event if oxides crystals were present. There is thus more dissolved water in the shallow part of the conduit of the transient model than in that of the Degruyter model. The effect of the separation of gas and liquid driving the shallow porosity reduction is dampened in the transient model by a slower rate of mass transfer compared to the forced equilibrium degassing of the Degruyter model, thus delaying porosity reduction.

Provided that D is high enough ($> 10^{-11}$ m^2/s), equilibrium degassing can thus be achieved by the transient model over most of the conduit to within 0.012 of φ^{eq}. Conduit ends, however, remain supersaturated with water, although not to a degree able to induce heterogeneous nucleation on any minerals commonly present in intermediate or silicic magmas.

The Degruyter model is a two-point boundary value system where the single pressure, p, is set at both conduit ends. The transient model also sets pressure at both boundaries but it considers two pressures. As they have close values (Figure 2A), it suffices to compare p_g and p. The interplay between the dynamic pressure controlled by u_l and the magmatic pressure controlled by φ causes p_g (and p) to depart from a linear pressure profile for both the Degruyter model and the transient model with $D > 10^{-11}$ m^2/s (Figure 3). Cases with $D = 10^{-13}$ and $D = 0$ m^2/s have nearly linear pressure profiles because φ is small over most of the conduit length (Figure 1).

Both models yield very similar distributions of total water content (Figure 4), velocities (Figure 5), and thus mass discharge rate (5.7 vs. 5.3×10^5 kg/s). For simplicity, we only use the transient model solution with D_{Ni} as a reference to characterize how water weight fractions change as a function of height in the conduit. The total water content at the inlet, C_T, is the same in both models (i.e. $C_T = C_c$, Section 5.3). In the Degruyter model, C_c is assumed constant along the conduit length. Figure 4 shows that C_T in both models have the same decreasing trend towards the surface, which indicates that total water content is in fact not constant along the conduit. That water mass conservation is not maintained is also apparent in the behavior of the ratios between exsolved water and total mass, n and n^{eq}, because they strongly diverge above 4.5 km. This divergence happens where u_g becomes much larger than u_l, decoupling outgassing from gas exsolution (Figure 5).

At the local scale of a single gas bubble, disequilibrium degassing has been characterized by different regimes of bubble growth [Lensky et al., 2004]. In a Lagrangian framework attached to one bubble, these regimes can be identified by two dimensionless parameters, Θ_D and Θ_V, that are linked respectively to the diffusion time scale $\tau_{\mathrm{dif}} = \frac{R_b^2}{D}$ and the viscous time scale $\tau_{\mathrm{vis}} = \frac{4\eta_{l0}}{p_{l0}}$, [Lensky et al., 2004, Forestier-Coste et al., 2012]:

$$\Theta_D = \frac{\tau_{\mathrm{dif}}}{\tau} = \frac{R_b^2}{\tau D} \quad \text{and} \quad \Theta_V = \frac{\tau_{\mathrm{vis}}}{\tau} = \frac{4\eta_{l0}}{\tau p_{l0}}, \tag{6.1}$$

where $\tau = p_l/\dot{P}$ is a characteristic time scale of pressure change and $\dot{P}$ is the local decompression rate given by (in an Eulerian framework):

$$\dot{P} = \partial_t p_l + u_l \partial_z p_l. \tag{6.2}$$

These characteristic times comes from the microscopic framework (see also Part I, Section 2.2 [Narbona-Reina et al., 2024]); τ_{dif} is the time for the Lagrangian of the concentration $\mathcal{C}$ (see equation 2.26 in [Narbona-Reina et al., 2024]) and τ_{vis} comes from the Rayleigh-Plesset equation for the bubble radius $\mathcal{R}$ (see equation 2.17 in [Narbona-Reina et al., 2024]).

In Part I, Section 4 [Narbona-Reina et al., 2024], we have proposed a scaling for the mass conservation (3.1b)–(3.1c) and the φ equation (6.8) below in drift-flux formulation. The Lagrangian scaling (6.1) can be related to our Eulerian scaling by assuming that the pressure changes are dominated by the vertical motion (u_l term in (6.2)) so that $\tau = L_0/u_0$, where L_0 and u_0 are the characteristic length and speed, respectively. In two-phase formulation (i.e. with

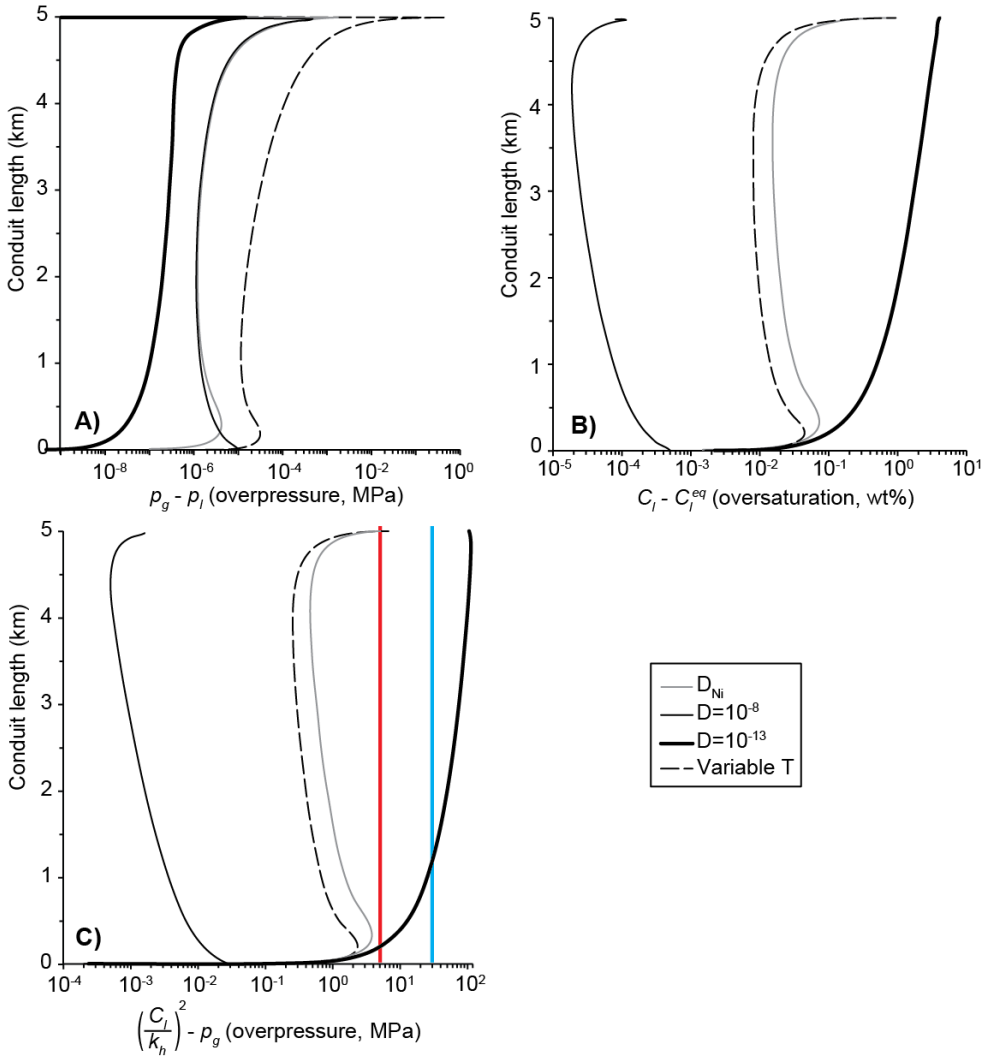

Figure 2: Measures of disequilibrium degassing as a function of height in the conduit for the transient model at steady state with several values of diffusion (isothermal) and D_{Ni} (variable, single temperature). A) Supersaturation pressure $(p_g - p_l)$. B) Oversaturation $(C_l - C_l^{\mathrm{eq}})$. C) Gas overpressure $\left|\left(\frac{C_l}{k_h}\right)^2 - p_g\right|$. The two vertical lines indicate approximate nucleation thresholds for oxides (red) and biotite (cyan).

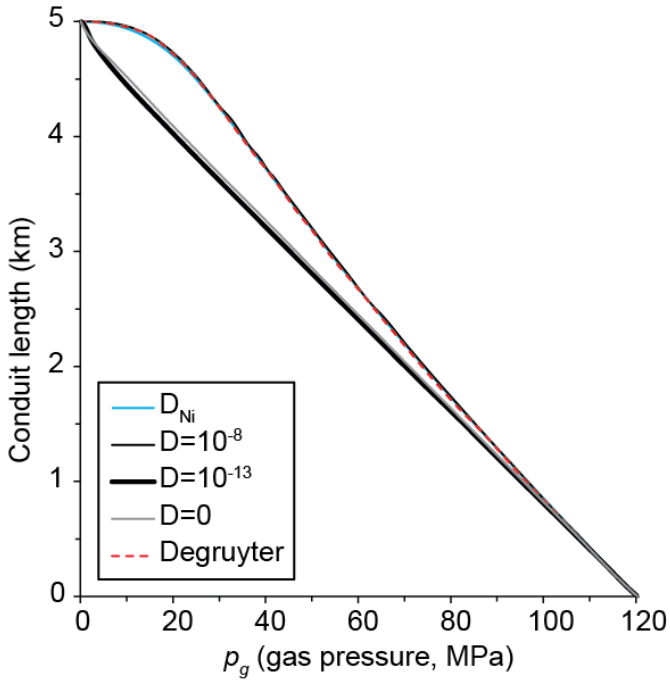

Figure 3: Gas pressure (p_g) as a function of height in the conduit for the Degruyter model and the transient model at steady state with several values of diffusion.

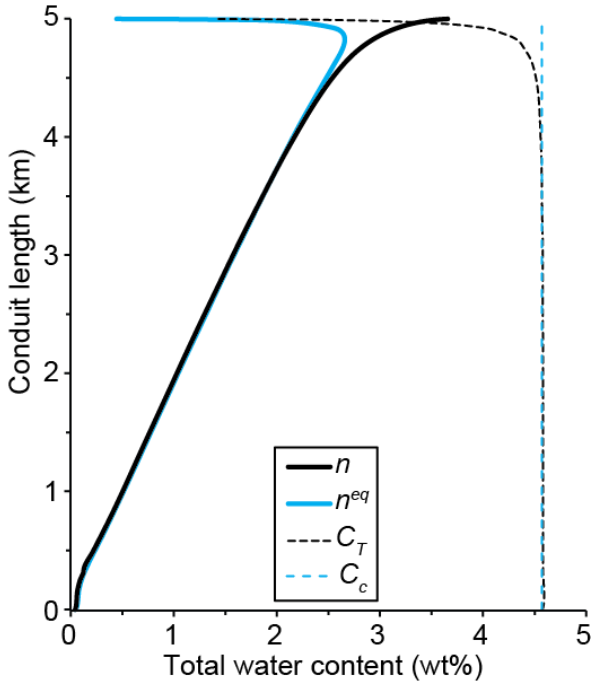

Figure 4: Various measures of water weight fraction as a function of height in the conduit for the Degruyter model (C_c) and the transient model with D_{Ni} at steady state (C_T, n, n^{eq}). Note that the three corresponding curves of the Degruyter model for C_T, n, and n^{eq} would overlap exactly those of the transient model at the scale of the figure.

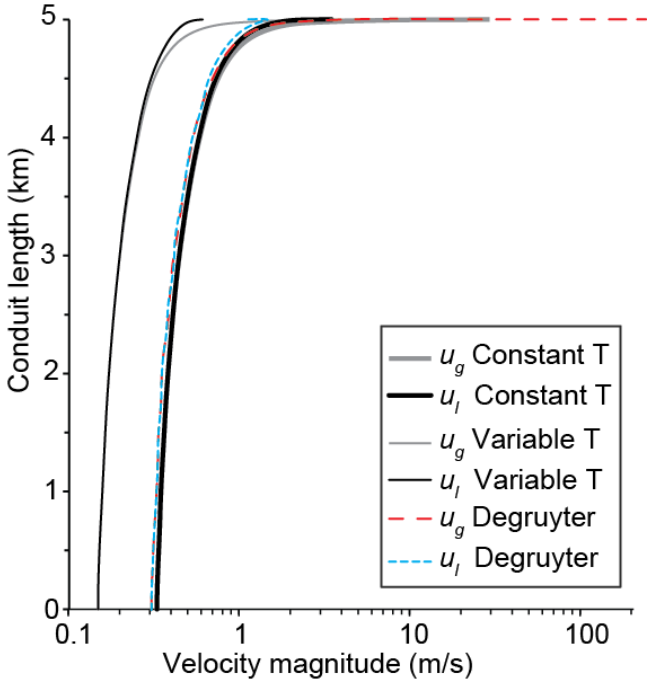

Figure 5: Gas (u_g) and liquid (u_l) velocities as a function of height in the conduit for the Degruyter model and the transient model with D_{Ni} at steady state with constant and variable, single temperature.

u_l and u_g), the dimensionless mass conservation (3.1b) and φ transport (6.8) can be expressed in terms of Θ_D and Θ_V:

$$\mathrm{St}\,\partial_{\tilde{t}}(1-\varphi) + \partial_{\tilde{z}}((1-\varphi)\tilde{u}_l) = -\mathrm{St}\,\frac{3C_{l0}}{\Theta_D}\,(\varphi^{2/3}\tilde{N})^{2/3}\frac{\tilde{C}_l - \sqrt{\tilde{p}_g}}{1-\varphi^{1/3}}$$

$$\mathrm{St}\,\partial_{\tilde{t}}\varphi + \tilde{u}_l\partial_{\tilde{z}}\varphi = \mathrm{St}\,\frac{3}{\Theta_V}\frac{\varphi(1-\varphi)}{\tilde{\eta}_l}\left(\frac{p_{g0}}{p_{l0}}\tilde{p}_g - \tilde{p}_l\right)$$

where the diacritic notation with a tilde is used for dimensionless variables (that is $\phi = \phi_0\tilde{\phi}$ where ϕ_0 is some reference value) and $\mathrm{St} = L_0/(u_0 t_0)$ is the Strouhal number. The Θ_D–Θ_V framework of [Forestier-Coste et al., 2012] can thus be used to characterize the bubble growth regimes occurring during ascent in our simulations.

Figure 6 shows that the large changes in D values yield broadly parallel paths in the Θ_D–Θ_V space because increasing D mostly shifts curves towards higher Θ_D. Focusing on the range of D values covered by D_{Ni} ($10^{-12} - 10^{-11}$ m^2/s), the run start at depth from the equilibrium regime, where $p_g = p_l$, $C_l = C_l^{\mathrm{eq}}$, and $\varphi = \varphi^{\mathrm{eq}}$. Within 500 m of the surface, runs approach a frozen state where the large melt viscosity and the large decompression rate of p_l cause both p_g and R_b to remain constant, increasing overpressure (Figure 2A). This last regime affects only the last few meters before the surface, resulting in a constant porosity (this is not visible at the scale of Figure 1B). At low diffusion (10^{-13} m^2/s), Θ_D is large (> 1) and mass transfer vanishes towards the surface. Conversely, at high D values, the competition between viscous forces hindering bubble growth and water diffusion fostering it remains fierce during the whole ascent. This indicates that, for this set of initial and boundary conditions, mass and momentum transfers occur constantly during ascent at natural diffusion values; the two-fluid system is far from limit cases during most of the ascent. This is consistent with the scaling of Part I, Section 4 [Narbona-Reina et al., 2024], which suggested that mass exchange is a major control of flow dynamics.

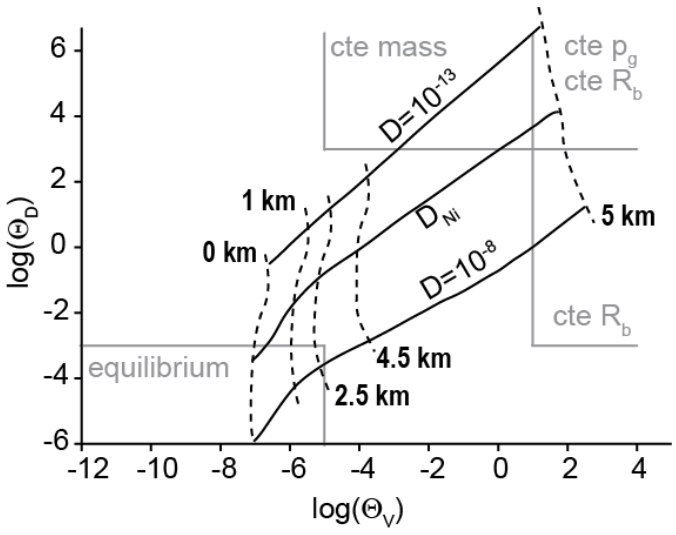

Figure 6: Viscous number (Θ_V) as a function of diffusion number (Θ_D) for several values of diffusion in the transient model at steady state. Gray labels and boundaries mark limit regimes [Forestier-Coste et al., 2012] and bold labels indicate positions along the conduit length.

Section 5 in Part I [Narbona-Reina et al., 2024] also proposes a simplification of the full two-phase system to obtain a relaxed system with respect to mass exchange, which means that one of the equilibrium degassing condition, $C_l = C_l^{eq}$, is always fulfilled everywhere. This relaxed system, however, is not isothermal. Further comparisons are thus carried out in the following section 6.1.2 that presents results with variable temperature.

6.1.2 Variable temperature

The energy equation of the Degruyter model (4.10) has residual terms outside the space derivative with no predetermined sign. We converted those terms, which have units of $\mathrm{J\,m^{-3}\,s^{-1}}$, into an equivalent temperature gradient of the liquid phase by dividing them by $c_{pn}u_n$ (see (2.15)). These converted terms indicate the cooling or heating per unit length that the liquid would have if the Degruyter model had variable temperature. A positive value means heating due to dissipation while a negative value implies cooling. Figure 7 shows the sum of these residual terms along the conduit length. The term with the largest absolute value is $\varphi u_g \partial_z p_g$ by far. That term causes the sum to be negative over most of the conduit. The neglected terms in the energy balance of the Degruyter model are thus not dissipative in the tested scenario.

As introduced in Section 2.2, the equation (2.15) is used in the single-temperature, transient model to replace (2.1g) and (2.1f) (or (3.1f) and (3.1g) in the 1.5D formulation). To compare steady-state solutions, we neglect the time derivative in (2.15), which yields an equation that breaks down the various contributions to the temperature gradient:

$$\partial_z T = \frac{\varphi}{c_{pn}u_n} u_g \partial_z p_g + \left((c_{pl} - c_{pg})T + \frac{p_l}{\rho_l} \right) \frac{R^{H_2O}}{c_{pn}u_n} + \frac{D_H}{c_{pn}u_n} \tag{6.3}$$

The terms on the right-hand side represent heating/cooling due to gas pressure changes, mass exchange, and shear heating, respectively. The terms giving dissipative contributions to the energy equation (3.8) are neglected in the temperature equations (2.15) and (6.3) (see the scaling in Part I, Section 4 [Narbona-Reina et al., 2024]). Here we calculate

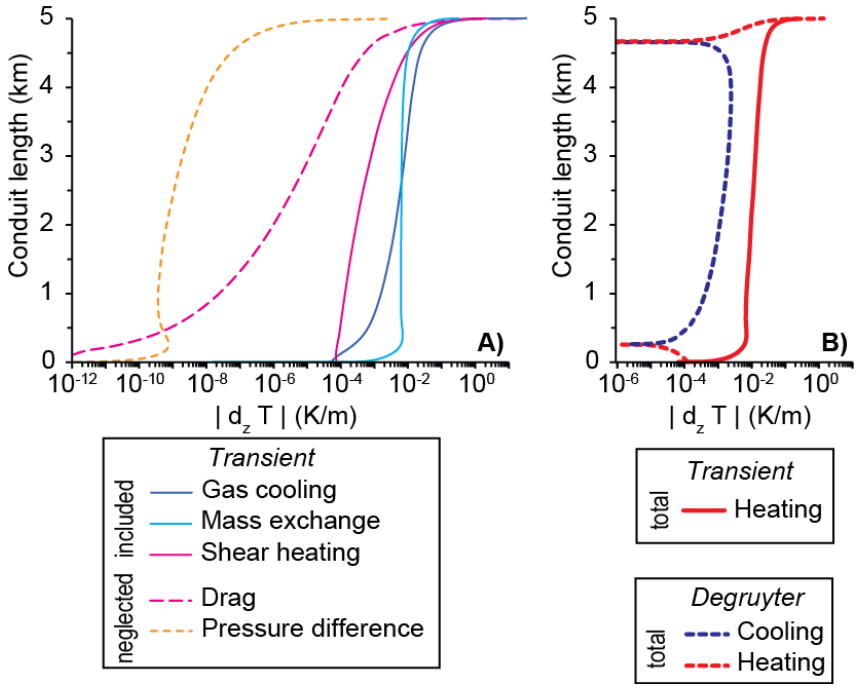

Figure 7: Absolute value of energy contributions ($|\partial_z T|$) as a function of height in the conduit for the Degruyter run and for the transient model with D_{Ni} at steady state. Hot colors indicate positive terms causing heating and cool colors indicate negative terms causing cooling. A) Breakdown of all the energy terms for the transient model. Dashed lines indicate terms neglected in the heat equation, thin solid lines indicate terms included into the heat equation. B) Total energy contribution.

these terms a posteriori to demonstrate the vanishing nature of their contribution to temperature changes. These neglected terms would be added to the right-hand side of (6.3) as, respectively, the drag, $\varphi(1-\varphi)K_d|u_g-u_l|^2/(c_{pn}u_n)$, and the viscous relaxation due to pressure difference, $3\varphi(1-\varphi)(p_g-p_l)^2/(4\eta_l c_{pn}u_n)$.

Focusing on the steady state solution with D_{Ni} and a single temperature, T, Figure 7A shows that, as expected, both neglected terms are positive and orders of magnitude smaller than the terms included in the energy balance (6.3). Of the included terms, the viscous dissipation due to shear heating is the smallest. The energy absorption due to mass exchange reaches a magnitude similar to that of the cooling due to gas decompression, which both reach large negative values near the surface. We can thus expect an overall cooling of the magma caused by gas exsolution and expansion in the transient model with variable, single temperature (Figure 7B). This effect would also appear in the Degruyter model if the isothermal assumption were removed, albeit to a lower degree (Figure 7B).

The energy balance of the transient model with a single temperature is thus dominated by gas expansion and exsolution at shallow level. Figure 8 shows that T decreases by ~ 72 K over the conduit length with most of the cooling occurring shallowly. Ignoring shear heating increases the cooling over the conduit length by ~ 30 K. We have considered two methods to take wall friction into the 1.5D model. The first keeps the two-phase nature of the model and assumes a wall friction and a corresponding viscous heating (3.2)–(3.3) that are functions of $1-\varphi$ and of the dilatational viscosity, $\eta_l/3$. The method has the disadvantage of yielding a progressively inviscid system as $\varphi \to 0$, which underestimates viscous heating when gas bubbles do not act as perfectly deformable objects [Llewellin et al., 2002]. The second approximation assumes that wall friction is that of a gas-free system, thereby overestimating shear heating but ignoring dilatational viscous heating (3.4)–(3.5). Figure 8 shows that keeping the gas-free friction (3.4)

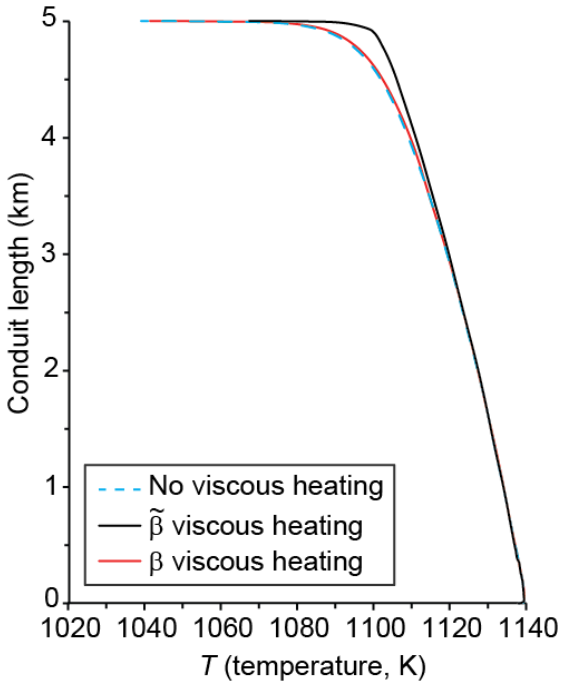

Figure 8: Effects of viscous dissipation on temperature (T) as a function of height in the conduit for the transient model with D_{Ni} and a single temperature at steady state. Cases are without viscous heating (blue dashed curve), with shear heating consistent with gas-free wall friction (black curve), and with viscous heating consistent with two-phase wall friction (red curve).

in the momentum equation but using the two-phase viscous heating (3.3) yields only 2.4 K of heating compared to no viscous dissipation, which reflects the moderating effect of the $1-\varphi$ factor. Interestingly, the dilatational term only accounts for $<$1% of the total viscous dissipation contribution, suggesting that neglecting it is acceptable. The viscous heating in a 3D case is thus likely to be framed by these two approximations of shear heating, which differ by a factor $(1-\varphi)/4$. Finally, the transient model with two temperatures (equations (3.1f) and (3.1g)) indicates that T_g is within 3×10^{-5} K of T_l. Thus, using a single-temperature model that neglects the energy dissipation due to drag, mass transfer, and dilatational viscosity is justified a posteriori.

The porosity evolution from depth is similar to that of the isothermal case except at shallow levels, where it is a few percent lower (Figure 1A). This is because cooling increases melt viscosity, which in turn decrease ascent velocities (Figure 5). The slower ascent rate compared to the isothermal case causes the largest change by reducing the mass discharge rate by a factor 2, from 5.7 to 2.9×10^5 kg/s. The lower ascent rate also gives more time for water diffusion to occur, lowering the degree of oversaturation (compare the grey and dashed curves in Figure 2B and C). The higher melt viscosity also affects gas pressure. The change would be indistinguishable at the conduit scale (Figure 3), but it is visible in the pressure difference p_g-p_l (Figure 2A) because cooling induces overpressures that are one order of magnitude higher than in the isothermal case.

In Part I, Section 4.3 [Narbona-Reina et al., 2024], we proposed a simplified two-phase system that only retains first-order terms. This scaling suggests that the drift velocity u_g-u_l can be captured by Darcy's law without gravitational effects:

$$u_g-u_l=-\frac{1}{(1-\varphi)K_d}\nabla p_g \tag{6.4}$$

Our results show that the ratio $-\partial_z p_g/((1-\varphi)K_d(u_g-u_l))$ is ~ 1 at the conduit ends and increases with a parabolic shape to a modest value of 2.8 in the middle of the conduit despite that the drift velocity spans many orders of magnitude (from 10^{-9} to 10 m/s). As explored in Section 6.1.4, equation (6.4) is a good first-order approximation of the gas momentum equation.

A novelty of the transient model is the presence of a exchange term R^{H_2O} that is a function of water diffusion and inter-bubble distance. It has the sought properties of tending towards zero at vanishing porosity and to infinity at vanishing inter-bubble distance, see Part I, Section 2.2.2 [Narbona-Reina et al., 2024]. Figure 9 shows different mass exchange terms from the literature compared to that of the transient model. We consider in particular the exchange proposed in [Lyakhovsky et al., 1996] and [Mancini et al., 2016] that are analyzed in Remark A.1 in Part I [Narbona-Reina et al., 2024] (with the Part I notation, the values $\mathcal{A}=1, \mathcal{R}_0=\mathcal{R}$ are considered for the [Mancini et al., 2016] case). They are, respectively,

$$R^L = \frac{1-\varphi}{\varphi^{1/3}(1-\frac{1}{2}\varphi^{2/3}-\frac{1}{2}\varphi^{1/3})}R^{H_2O}, \qquad R^M = \frac{1}{3}\frac{(1-\varphi)(1-\varphi^{1/3})}{\varphi^{4/3}}R^{H_2O}.$$

All these exchange terms (including that from the Degruyter model) were recalculated from the steady-state solution of the transient model with D_{Ni} and a single temperature. As expected, the equilibrium exchange rate of [Degruyter et al., 2012] is orders of magnitude larger than the other, diffusion-based terms. All the other rates have very similar values at the conduit mid-length, and the [Lyakhovsky et al., 1996] rate is close to R^{H_2O}.

These exchange terms estimate mass transfer between the melt cell and a bubble by simplifications of the concentration profile within the melt cell. Our formulation of R^{H_2O}, for instance, is done by a Taylor expansion that omits higher order terms (Section 2.2.2 in [Narbona-Reina et al., 2024]). Figure 9 shows the mass transfer given by the microscopic bubble growth model of [Forestier-Coste et al., 2012] as implemented by [Mancini et al., 2016], which solves for the water concentration from the bubble wall to the edge of a melt cell. This microscopic Lagrangian model includes the viscous relaxation governed by the Rayleigh-Plesset equation, but, unlike the transient model, it is isothermal and assumes closed-system degassing (i.e. no gas escape from the bubbles). It was initialized with the same parameters as the transient model (Table 2, D_{Ni}, and η_l according to (2.6c)) and it was constrained at each time increment by the decompression rate given by the steady-state solution of the transient model. Although the linearized concentration profile can be far from the full solution of the diffusion equation with a moving boundary (see [Mancini et al., 2016] for a comparison covering a wide portion of the $\Theta_V-\Theta_D$ space), Figure 9 shows that R^{H_2O} closely follows the mass transfer of the microscopic model despite their inherent differences (constant vs. inconstant temperature and closed vs. open system, respectively). The last hundred meters or so of the ascent is missing from the microscopic model solution because the closed-system assumption yields large porosities at low pressure. Calculations were stopped when φ reached 0.75 as, beyond that value, the microscopic bubble size would have largely been overestimated compared to that of the transient model.

The exchange term of [La Spina and de' Michieli Vitturi, 2012] and [La Spina et al., 2017] does not involve diffusion:

$$R^{LS} = \frac{(1-\varphi)\rho_l}{\tau^{(d)}}(C_l - k_h\sqrt{p_g})$$

where $\tau^{(d)}$ is a time constant (see Section 6 in Part I [Narbona-Reina et al., 2024]). Instead of assuming a single $\tau^{(d)}$ value, we calculated the expected $\tau^{(d)}$ evolution from our model outputs. Figure 9B shows that the equivalent time constant for diffusion D_{Ni} varies from 0.03 to 0.5 s in our run.

In Part I, Section 6, [Narbona-Reina et al., 2024], we proposed a relaxed system with one velocity, u_T (2.13), and

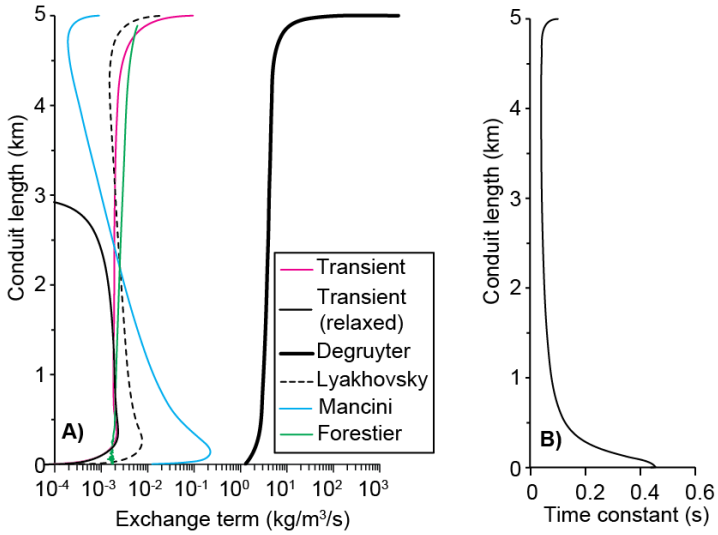

Figure 9: Mass exchange factors as a function of height in the conduit for the transient model with D_{Ni} and a single temperature at steady state. A) Full exchange terms. B) Time constant $\tau^{(d)}$ in [La Spina et al., 2017]

one temperature, T. This system assumes that $C_l = C_l^{eq}$ and its dilatancy expression in 3D is:

$$(\mathrm{div} u_T)_{relax} = -\frac{1}{\mathcal{A}} \frac{3\varphi}{4\eta_l}(p_g - p_l) + \frac{\varphi}{2Tc_{pm}\mathcal{N}_s} \mathcal{D} : \nabla u_T \tag{6.5}$$

where

$$\mathcal{N}_s = \varphi - \frac{1}{2}\left(1 - \frac{\rho}{\rho_g}\right)\left(1 + \frac{\varphi c_{vg}\rho_g}{c_{pm}}\right) - \frac{\varphi(1-\varphi)}{2Tc_{pm}}(c_{pg}\rho_g T - p_l - c_{pl}\rho_l T),$$

c_{pm} is defined in (2.13), and $\mathcal{A}$ and $\mathcal{D}$ will be simplified in the subsequent calculations but their expressions can be found in [Narbona-Reina et al., 2024]. Equation (2.4), on the other hand, gives the 3D dilatancy of our system:

$$\mathrm{div} u_l = \frac{3\varphi}{4\eta_l}(p_g - p_l) - \frac{R^{H_2O}}{\rho_l(1-\varphi)}. \tag{6.6}$$

In most of the conduit, $u_g - u_l$ is small. In particular, in the part <3 km, the bulk velocity u_T follows closely u_l such that $\partial_z u_T$ is within 3% of $\partial_z u_l$. We can thus compare our system and the single velocity, relaxed system in the lower part of the ascent. Equating the 1.5D simplifications of the two dilatancy equations (6.5)–(6.6) yields an expression for the equivalent mass exchange, $R^{H_2O}_{relax}$, that the system would have if it were relaxed. Assuming that $u_T = u_l$ and using (2.3), the 1.5D dimension reduction yields $\mathcal{D} : \nabla u_T \approx 2u_l(1-\varphi)\eta_l / r_c^2$. Taking into account that $\mathcal{A} \approx 1$ [Narbona-Reina et al., 2024], this relaxed exchange term is:

$$R^{H_2O}_{relax} \approx \frac{\varphi(1-\varphi)^2 \rho_l \eta_l u_l}{2Tc_{pm}\mathcal{N}_s r_c^2}. \tag{6.7}$$

Figure 9A shows that $R^{H_2O}_{relax}$ is within 5% of R^{H_2O} during the first km of ascent, which is consistent with the equilibrium assessment done with Θ_D–Θ_V in isothermal conditions (Figure 6).

6.1.3 Alternate outlet boundary condition

The physical processes occurring at the outlet can be understood by considering the transport equation on porosity that can be built from the equation system using (2.1a) and the Rayleigh-Plesset equation (2.4), see Part I, Section

2.3 [Narbona-Reina et al., 2024]:

$$\begin{aligned}\partial_t\varphi + u_l\partial_z\varphi &= \frac{3}{4\eta_l}\varphi(1-\varphi)(p_g - p_l)\\ &= (1-\varphi)\partial_z u_l + \frac{R^{H_2O}}{\rho_l}\end{aligned} \tag{6.8}$$

When the outlet boundary condition of equal pressures (5.8a) is used, it also implies that $\partial_t\varphi + u_l\partial_z\varphi = 0$ at the outlet because of (6.8). In other words, forcing no exsolution and no liquid acceleration at the outlet causes φ to become a transported quantity at that location. This is often not desirable because, in natural conditions, the position of an outlet (i.e. the vent) is not correlated with a sudden absence of water exsolution. In other words, there are generally no physical reasons to assume that $(R^{H_2O})_{|\Gamma_{\text{out}}} = 0$.

When relaxing equal pressures at the outlet and setting instead $(p_g)_{|\Gamma_{\text{out}}} = p_{\text{top}}$ and $(p_l)_{|\Gamma_{\text{out}}}$ given by (5.8b), almost identical steady-state, variable temperature results are obtained on all variables but p_l. This difference in the p_l distribution is best understood by tracking $p_g - p_l$ (Figure 2A). As near the outlet the liquid is accelerating and gas exsolution occurs, one can expect that $(p_l)_{|\Gamma_{\text{out}}} < p_{\text{top}}$. Now, p_{top} being set to the (rather small) atmospheric value of 0.1 MPa, both acceleration and exsolution cause $(p_l)_{|\Gamma_{\text{out}}}$ to reach the negative value of -5 MPa (Figure 10). Using the averaged pressure condition with $(\varphi p_g + (1-\varphi)p_l)_{|\Gamma_{\text{out}}} = p_{\text{top}}$ given by (5.8c) reduces the pressure difference at the outlet but does not alleviate negative p_l values: $(p_l)_{|\Gamma_{\text{out}}} = -1.26$ MPa and $(p_g)_{|\Gamma_{\text{out}}} = 0.6$ MPa. These nonphysical results are linked to the breakdown of the 1.5D conduit geometry at the outlet; a realistic simulation of an effusive eruption with atmospheric gas pressure at the outlet needs to take the free surface of the liquid into account.

One way to set realistic outlet conditions in a 1.5D geometry is to consider that the cylindrical conduit is topped by a magma accumulation (such as a dome) that increases the upper boundary pressure. A simple example without magma accumulation above the upper boundary would be a 100-m thick overburden that causes $p_{\text{top}} = 2.5$ MPa. Runs done with $(p_g)_{|\Gamma_{\text{out}}} = (p_l)_{|\Gamma_{\text{out}}} = 2.5$ MPa and runs done with the alternate outlet boundary conditions (5.8b) and (5.8c) yield again almost identical steady-state results on all the variables but p_l, which has the realistic outlet value of 1.91 MPa with (5.8b) and 2.36 MPa with (5.8b) ($(p_g)_{|\Gamma_{\text{out}}} = 2.57$ MPa in that last case). Compared to the variable temperature solutions with no overburden, the addition of an overburden increases the mass discharge rate from 2.9 to 3.4×10^5 kg/s regardless of the outlet pressure condition but yields similar trends as those shown in Figures 1–5.

6.1.4 Simplified system

In steady state, the largest change induced by our expression of the energy balance is a reduction of the mass discharge rate by a factor 2 compared to the isothermal case. This reduction is caused by the increased viscosity due to melt cooling. Although temperature variations cannot be ignored, some simplifications do not affect much the steady-state mass discharge rate. We assess the impact of neglecting various physical processes to find the minimum model that still captures the essential physics of steady state magma ascent. We use the mass discharge rate:

$$Q = \pi r_c^2\Big(\varphi\rho_g u_g + (1-\varphi)\rho_l u_l\Big)$$

as a diagnostic quantity because it can be shown by adding (2.1a) and (2.1b) that Q is constant in steady state (Remark 2.1 in [Narbona-Reina et al., 2024]).

The physical processes considered are shear heating, liquid inertia, mass exchange, and permeable flow. Taking shear heating into account in the temperature equation increases the mass discharge rate by 13 %. A run with the transient model using (6.4) instead of (3.1e) increases the mass discharge rate from 2.9 to 3.2×10^5 kg/s (8 %). Omitting the R^{H_2O} and inertial terms in the momentum equations (3.1d)-(3.1e) and the R^{H_2O} term in the p_l equation

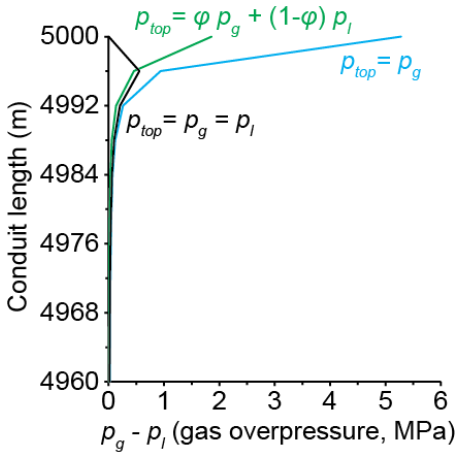

Figure 10: Gas overpressure with respect to the liquid pressure ($p_g - p_l$) in the upper part of the conduit for the transient model at steady state with D_{Ni}, a single temperature, and an outlet pressure of 0.1 MPa. The outlet has either an imposed pressure equality (black, $p_{\mathrm{top}} = p_g = p_l$), or a liquid pressure controlled by dilatancy (cyan, $p_{\mathrm{top}} = p_g$), or an imposed average pressure (green, $p_{\mathrm{top}} = \varphi p_g + (1-\varphi) p_l$).

(3.1i) decreases mass discharge rate by only 0.1%. These four physical processes have thus relatively low influence on Q and thus could potentially be neglected to obtain a simplified system.

As φ is generally small at the conduit inlet, we use the scaling variable $Q_0 = \rho_{l0} \pi r_c^2 u_0 \sim Q_{|\Gamma_{in}}$. We relax the constraint of energy dissipation and we arbitrarily set that the Q_0 of the simplified system should remain within 10% of that of the full system.

As we have explored only a small subset of conduit conditions (Table 2), we use the dimensionless analysis of Section 4.3 of [Narbona-Reina et al., 2024]) to design regime diagrams. We start each analysis by assuming that the dimensionless number of interest should be much lower that the equation leading-order term(s). We then use the steady-state solution of the transient model with D_{Ni} and a single temperature (e.g., Figure 9) to determine the actual threshold value(s) of that dimensionless number beyond which physical processes could be neglected. Finally, the thresholds are used to map the dynamical regimes over a wide range of natural parameters.

The dimensionless factor of the shear heating term is $F_{sh} = \eta_{l0} u_0 / (\rho_{l0} L_0 T_0 C_{pl})$. Figure 11A shows that it is well below 1 over the whole ascent despite that shear heating affects mass discharge rate by >10%. To determine the actual threshold below which shear heating can be neglected, we use the condition that the mass discharge rate without shear heating, $Q_1 = \rho_{l0} \pi r_c^2 u_1$, should be within 10% of the reference rate Q_0:

$$f = 0.1 = \frac{Q_1 - Q_0}{Q_0} = \frac{u_1}{u_0} - 1.$$

To the main order (Section 4.3 of [Narbona-Reina et al., 2024]), the liquid speed is proportional to η_l because the flow can be approximated by the Poiseuille equation (i.e. an incompressible Newtonian fluid flowing in a laminar fashion through a cylindrical pipe of constant radius). So $u_1/u_0 \approx \eta_{l1}/\eta_{l0}$ and

$$\partial_T (\log_{10} \eta_l) \sim \frac{\eta_{l1} - \eta_{l0}}{\Delta T} \frac{\log_{10} e}{\eta_{l0}} \sim \frac{\log_{10} e}{\Delta T} \left(\frac{u_1}{u_0} - 1 \right) = \frac{\log_{10} e}{\Delta T} f$$

where ΔT is the temperature difference between the two cases. In other words,

$$\Delta T = \frac{f \log_{10} e}{\partial_T (\log_{10} \eta_l)}$$

is the maximum temperature difference beyond which liquid heating (or cooling) causes mass discharge rate fluctuation in excess of $100f$ %. In the comparison shown on Figure 8, evaluation of ΔT with $f = 0.1$ and $\tilde{\beta}$ yields $3 - 5$ K. This range of ΔT occurs around $20 - 30$ MPa, which corresponds to a F_{sh} range of $1.4 - 2.4 \times 10^{-6}$ (Figure 11A). The number of degrees of freedom controlling F_{sh} can be reduced by relating η_{l0} to p_0 by using (2.6c) and (4.5). Using that relationship, Figure 11A shows that two extreme values of u_0 frame the behavior of F_{sh} as a function of pressure (Table 3). As these extreme value are only an order of magnitude apart, F_{sh} changes during ascent are mostly due to η_{l0}, the variation of which spans several orders of magnitude. Converting u_0 to Q_0 and using the threshold values of F_{sh}, Figure 11B shows the maximum η_{l0} values below which shear heating can be neglected for a range of natural Q_0 values.

Parameter	minimum	maximum
u_0	0.1	1
w_0	10^{-9}	10
η_{l0}	10^4	10^8
ρ_{l0}	2450	2450
L_0	30	30
T_0	1138	1138
p_0	0.1×10^6	120×10^6

Table 3: Scaling variables and their ranges in the transient run.

By convention, the scaling analysis yields dimensionless numbers such that the inertial term of the momentum equation is $O(1)$ (i.e. there is a factor 1 in front of $\partial_{\tilde{z}}((1-\varphi)\tilde{\rho}_l \tilde{u}_l^2)$ in the dimensionless version of (3.1d)). To decide whether this term can be neglected, it needs to be compared to the other terms of the momentum equation. Focusing on the two largest terms that survive at the main order, the pressure gradient and the viscous resistance term, one can multiply the dimensionless momentum equation (see Section 4.3 and the mixture velocity equation in Appendix E of [Narbona-Reina et al., 2024]) by either Ma^2, where $Ma^2 = \rho_{l0} u_0^2 / p_0$ is the Mach number, or by Re, where $Re = \rho_{l0} u_0 L_0 / \eta_{l0}$ is the Reynolds number, respectively, to evaluate whether the inertial term can be neglected.

Figure 11C shows that the inertial term can be neglected if $Ma^2 < 0.1$ and $Re < 5$. It also suggests that Ma changes during ascent mostly because of p_0, u_0 playing a subordinate role. Using the same reasoning as for F_{sh}, Re changes during ascent are mostly due to η_{l0} with u_0 also playing a minor role in controlling Re as a function of pressure. Converting u_0 in Q_0, Figure 11D suggests that inertial terms can only be neglected if $Q < 3 \times 10^6$ kg/s and at progressively lower liquid viscosity below that mass discharge rate.

The same reasoning and accompanying multiplication by either Ma^2, or $F_K = k_0 u_0^2 \rho_{l0} / (\eta_{g0} L_0 w_0)$ with the weighed drift velocity equation on $u_g - u_l$ (velocity equation on Yw in Appendix E of [Narbona-Reina et al., 2024]) yields dimensionless parameters that can be grouped in 3 distinct factors for each scaling: $F_{m1} = w_0 u_0 / (T_0 c_0)$, $F_{m2} = w_0^2 / (T_0 c_0)$, and $F_{m3} = \eta_{l0} u_0 / (\rho_{l0} L_0 c_0 T_0)$ for Ma^2 and $F_{k1} = p_0 u_0 k_0 / (T_0 c_0 \eta_{g0} L_0)$, $F_{k2} = p_0 w_0 k_0 / (T_0 c_0 \eta_{g0} L_0)$, and $F_{k3} = p_0 \eta_{l0} u_0 k_0 / (\rho_{l0} L_0^2 c_0 T_0 \eta_{g0} w_0)$ for F_K.

Figure 11E shows how these 6 factors change during ascent. The largest factor is either F_{m3}, or F_{k3}, with a common threshold of 0.1. In the case of F_{m3}, and considering the parameters kept constant in this analysis (Table 3), there is

a direct relationship between η_{l0} and Q_0 that is shown in Figure 11F. In the case of F_{k3}, the maximum viscosity below which Darcy's law (6.4) is valid is:

$$\eta_{l0} = F_{k3}\frac{4\rho_{l0}^2 T_0 c_0 L_0^4 \eta_{g0}}{\pi Q_0}\frac{w_0}{k_0 p_0}.$$

Considering the parameters kept constant in Table 3 and setting $F_{k3} = 0.1$, η_{l0} depends on Q_0 and on the dimensional quantity $w_0/(k_0 p_0)$. Figure 11F shows this maximum viscosity for 3 representative values of $w_0/(k_0 p_0)$: 1 (e.g., $w_0 = 10^{-6}$ m/s, $k_0 = 10^{-14}$ m^2, $p_0 = 100$ MPa), 10^2 (e.g., 0.01 m/s, 10^{-12} m^2, 100 MPa), and 10^4 (e.g., 10 m/s, 10^{-10} m^2, 10 MPa). Overall, Figure 11F suggests that the drift velocity equation (6.4) is valid over the whole range of mass discharge rates when $\eta_{l0} < 10^4$ and when $\eta_{l0} < 10^8$ and $w_0/(k_0 p_0) \geq 10^4$.

Remark 6.1. *The maximum values of w_0 considered in Table 3 might imply that the Darcian permeability relationship* (2.6)*, which only takes viscous effects into account, should be extended to a generalized Forchheimer relationship that includes the inertial effects caused by gas recirculation within the microscopic cavities of the bubble network (e.g., [Ruth and Ma, 1992]; [Degruyter et al., 2012]):*

$$K_{d(Fo)} = \frac{\eta_g}{k} + \frac{\rho_g}{k_2}|u_g - u_l|$$

where k_2 is an inertial permeability coefficient that quantifies how the geometry of the permeable network alters the gas velocity and pressure distributions. As a result, the linear Darcy interaction (6.4) *between gas and liquid becomes quadratic at large drift velocities. This generalized Forchheimer relationship is dominated by the inertial effects when $p_0 w_0 k_0/(\eta_{g0} c_0 T_0 k_{20}) \gg 1$, where k_{20} is a reference inertial permeability coefficient.*

The dimensionless factor of the R^{H_2O} terms in the momentum equations (3.1d)-(3.1e) and p_l equation (3.1i) is $F_r = p_0 w_0/(\rho_{l0} u_0 c_0 T_0)$. Figure 11G shows that F_r is well below 1 over the whole ascent, which is consistent with the fact that neglecting those terms does not affect much the mass discharge rate. It also suggests that w_0 and p_0 are the strongest controls of F_r. Assuming a F_r threshold of 0.1, Figure 11H shows the maximum values of w_0 as a function of Q_0 for characteristic values of p_0. Neglecting the contribution of mass transfer in the momentum and p_l equations is thus possible over the whole range of mass discharge rates for $w_0 < 0.01$ m/s at low pressure. At high pressure, where porosity is low and $k \sim 10^{-13} - 10^{-15}$ m^2, Darcy's law (6.4) suggests that $w_0 \sim 10^{-6} - 10^{-4}$ m/s. As a result, mass transfer terms can be neglected for $Q_0 > 10^3$ kg/s at high pressure.

Although a more complete parametric study is needed to explore the consequences of varying the parameters kept constant in this analysis (Table 3), we can propose a minimal set of equations by cumulating all the above simplifications. Omitting shear heating and the inertial and mass exchange terms in the liquid momentum equation, using Darcy's law to calculate u_g, and ignoring mass exchange in the dilatancy equation yields a simplified system that can approximate the steady-state mass discharge rate of the full system within 10% if the conditions shown in Figure 11B-D-F-H are simultaneously fulfilled:

$$\partial_t((1-\varphi)(1-C_l)) + \partial_z((1-\varphi)(1-C_l)u_l) = 0 \tag{6.9a}$$

$$\partial_t((1-\varphi)\rho_l) + \partial_z((1-\varphi)\rho_l u_l) = -R^{H_2O} \tag{6.9b}$$

$$\partial_t(\varphi\rho_g) + \partial_z(\varphi\rho_g u_g) = R^{H_2O} \tag{6.9c}$$

$$\partial_t((1-\varphi)\rho_l u_l) + \partial_z\left((1-\varphi)p_l\right) + \tilde{\beta}u_l - p_g\partial_z(1-\varphi) - K_d\,\varphi(1-\varphi)(u_g - u_l) = (1-\varphi)\rho_l g \tag{6.9d}$$

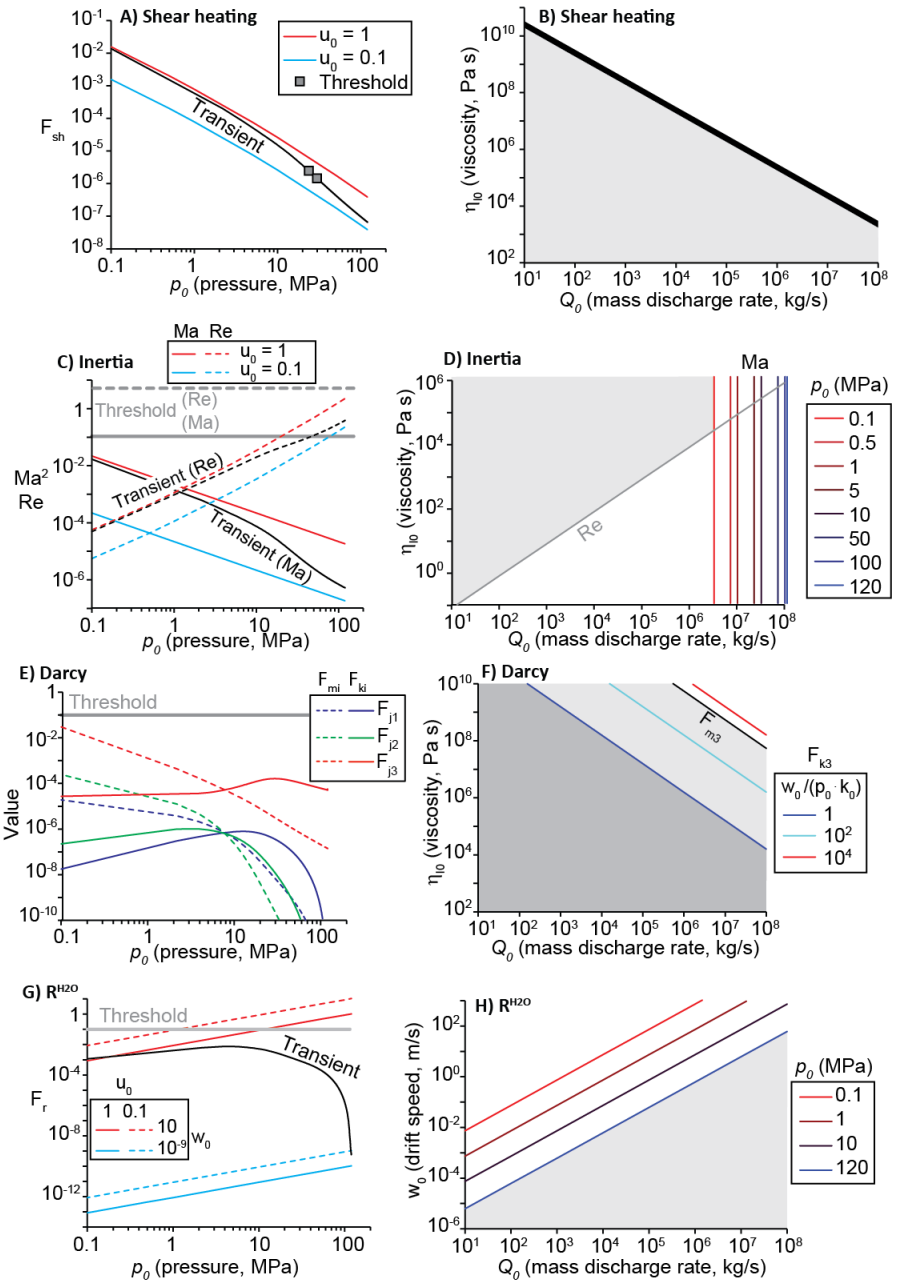

Figure 11: Scaling analysis and regime diagrams. A), C), E), G) Dimensionless parameters as a function of pressure for the transient run with D_{Ni} and a single temperature (black curves). Individual threshold values are shown as gray symbols or gray horizontal lines. B), D), F) Threshold liquid viscosity (η_{l0}) as a function of mass discharge rate (Q_0). H) Threshold drift speed (w_0) as a function of Q_0. A) Shear heating scaling (F_{sh}). Red and blue curves frame the transient run for extreme velocities (u_0). B) The gray area indicates where shear heating can be neglected. C) Liquid inertia scaling (Ma, Re). Red and blue curves frame the transient run for extreme u_0 values. D) The gray area shows the parameter space where liquid inertia can be neglected. The vertical colored lines represent various pressures (p_0) if the pressure gradient dominates the momentum equation (Ma). The gray line is valid if viscous stresses dominate the momentum equation (Re). E) Darcy scaling. Curves represent the scaling parameters (F_{ij}). F) Gray areas indicate where Darcy's equation is valid when viscous resistance (F_{k3}, dark gray) or inertia (F_{m3}, dark and light gray) dominates. G) Mass exchange scaling (F_r). Red and blue curves frame the transient run for extreme u_0 and w_0 values. H) The gray area indicates where liquid inertia can be neglected.

$$u_g = u_l - \frac{1}{(1-\varphi)K_d}\partial_z p_g \tag{6.9e}$$

$$c_{pm}(\partial_t T + u_T \partial_z T) + p_g \partial_z(\varphi u_g + (1-\varphi)u_l) + (c_{vg} - c_{pl})T R^{H_2O} = -\frac{4\eta_l}{3\varphi\rho_l} R^{H_2O} \partial_z u_l \tag{6.9f}$$

$$p_g = c_0 \rho_g T \tag{6.9g}$$

$$p_l = p_g - \frac{4\eta_l}{3\varphi}\partial_z u_l \tag{6.9h}$$

Importantly, this simplified system (6.9) no longer guarantees energy dissipation (Appendix B). The only term that could be neglected while ensuring energy dissipation is the shear heating term.

6.2 Transient behavior

Reaching steady state from an initial condition with a porosity increasing linearly along the conduit length takes time because of disequilibrium degassing. Steady state solutions feature small differences between p_g and p_l so that gas overpressure is not the limiting factor. Dissolved water, however, follows mass conservation and its distribution is controlled by a combination of advection by u_l and exsolution through R^{H_2O}. The initialization of C_l at C_l^{eq} can thus be far from the steady-state values, which can only be reached when C_l has been advected over the whole length of the conduit. This advection can easily be seen when diffusion is small, such as $D = 10^{-13}$ m^2/s (Figure 12A).

The inlet speed in steady state for the $D = 10^{-13}$ m^2/s run is ~ 1 m/s, and thus 76 min are needed for a magma batch to cover the 5 km of the conduit length assuming constant speed. This calculation gives an estimate of how long it takes for steady state to be established. A more precise ascent time can be obtained by integrating the liquid travel time across each computational node, which yields an integrated ascent time of 72 min (absolute times are also reported as fraction of this integrated time). The stationary solution yields differences with the transient solution at 76 min of $< 10\%$ on φ and $< 5\%$ on the other variables (C_l, p_g, p_l, u_l, u_g, and T). These differences between transient and steady states decrease to $< 2\%$ when the transient solution reaches 150 min. The transient solutions at the transfer time of $H/(u_l)_{|\Gamma_{\mathrm{in}}}$ thus offer a good representation of steady state. This is likely to be true under most conditions because u_l tends to increase towards the surface, making the transfer time based on the inlet velocity a minimum estimate.

The effect of C_l advection on the porosity evolution is shown in Figure 12B. The transition between the constant value of C_l advected from the conduit base and the initial C_l distribution causes a kink in porosity. This kink migrates from 1 km at 33 min to 2 km at 50 min and to 3.5 km at 67 min. It is no longer apparent in the quasi-steady-state solution at 72 min because it has been advected past the shallowest part of the conduit.

An interesting and persistent behavior occurs at higher D values. Figure 13 shows porosity losses at shallow depth and early times. This loss is due to a complex interplay between gas/liquid separation and exsolution. This low porosity region is transient with D_{Ni}, disappearing after 17 min to yield a monotonous porosity increase over the whole conduit length that eventually reaches steady state after ~ 6 h because the average ascent rate is ~ 0.2 m/s (Figure 13A). The low porosity region is more marked at high D values and causes the system to be sensitive to initial conditions, sometimes hindering the progression from a given set of initial conditions to steady state (Figure 13B). This temporary porosity drop is not due to numerical instabilities (it persists with a much finer grid, see Appendix A) and its origin lies in disequilibrium degassing.

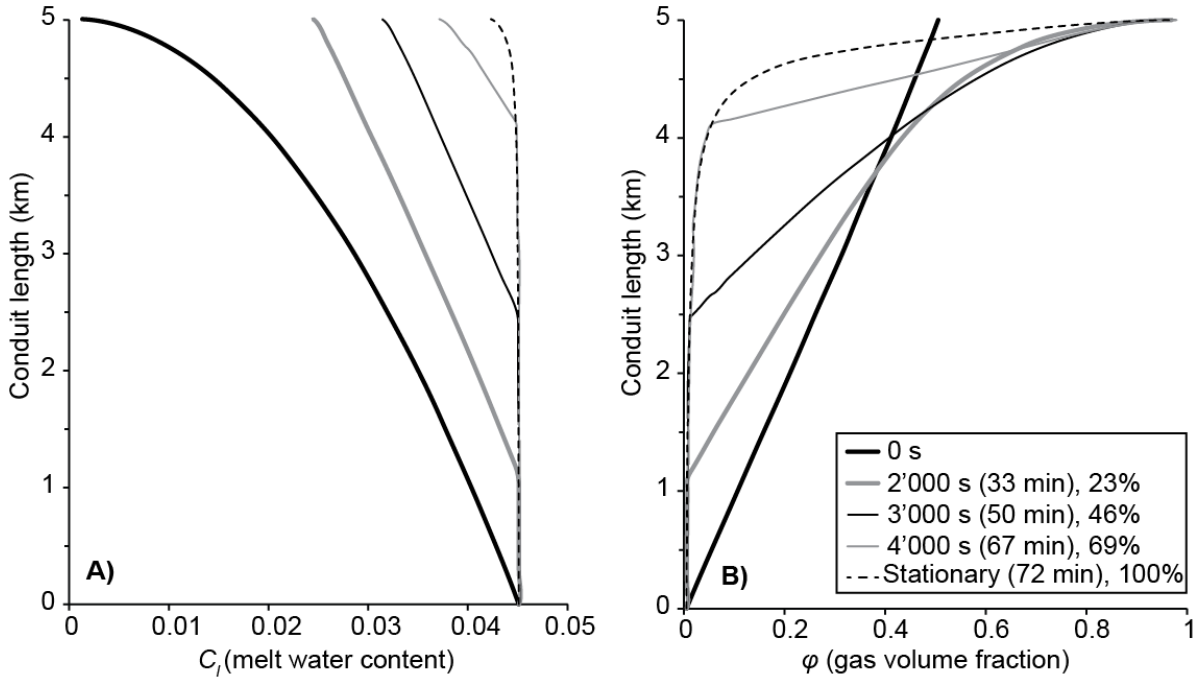

Figure 12: Temporal outputs from the transient model with $D = 10^{-13}$ m^2/s and a single temperature. Times are also indicated in fraction of total ascent time of the liquid at steady state. The difference between the solution at 72 min and the stationary solution is not apparent at the figure scale. A) Dissolved water content (C_l). B) Gas volume fraction (φ)

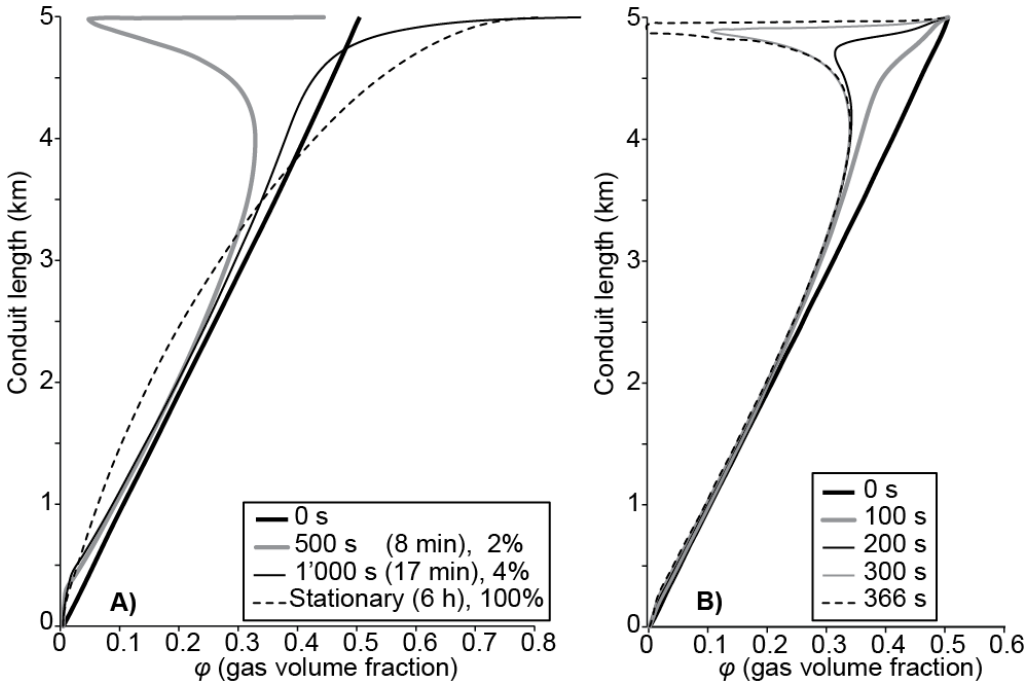

Figure 13: Gas volume fraction (φ) as a function of height in the conduit for different times of the transient model with a single temperature. Times are also indicated in fraction of total ascent time of the liquid at steady state. A) D_{Ni}. B) $D = 10^{-8}\ \mathrm{m}^2/\mathrm{s}$.

The behavior of the initial porosity loss is best understood with the transport equation on porosity (6.8):

$$\begin{aligned}\partial_t\varphi + u_l\partial_z\varphi &= \frac{3}{4\eta_l}\varphi(1-\varphi)(p_g - p_l)\\ &= (1-\varphi)\partial_z u_l + \frac{R^{H_2O}}{\rho_l}\end{aligned}$$

The low porosity region corresponds to vanishing u_l, which suggests that the porosity loss can be understood by only looking at the right-hand-side terms. Unlike in the case of steady-state solutions (Figure 2), the term R^{H_2O}/ρ_l is the smallest of the three terms on the right-hand sides of (6.8). In other words, the behavior of porosity at shallow level shown in Figure 13 is due to gas underpressure instead of supersaturation like in the steady-state case. More precisely, what controls porosity reduction is the product $\varphi(1-\varphi)(p_g - p_l)$, which is minimized when $\varphi \sim 0.5$ and $p_g < p_l$. The gas underpressure is a consequence of gas escape towards the outlet because of the large permeability at moderate and high φ, which causes $u_g > u_l$ and, in turn, $p_g < p_l$. The porosity loss is thus a consequence of efficient liquid–gas separation near the vent.

All steady-state solutions presented in Section 6.1 except that with $D = 10^{-8}\ \mathrm{m}^2/\mathrm{s}$ were obtained by starting from an initial linear porosity profile reaching 50 vol% at the surface (i.e. $\varphi_0 = 0.5$, Figure 13A). The case with $D = 10^{-8}\ \mathrm{m}^2/\mathrm{s}$ yields a porosity loss such that φ reaches 0 at a depth of a few tens of meters (Figure 13B). This creates an impermeable plug where $u_l \to 0$. Exploring this transient regime is beyond the scope of this inter-model comparison focused on steady states, but, once $\varphi \sim 0$ at one computational cell around 360 s, further calculations to ~ 366 s show that this region of vanishing porosity extends vertically, increasing plug thickness. This thickening occurs because the gas above the plug is being expelled towards the surface (i.e. $u_g \geq u_l$), which maintains gas underpressure almost all the way to the surface (it vanishes at the outlet according to the boundary condition (5.8a)).

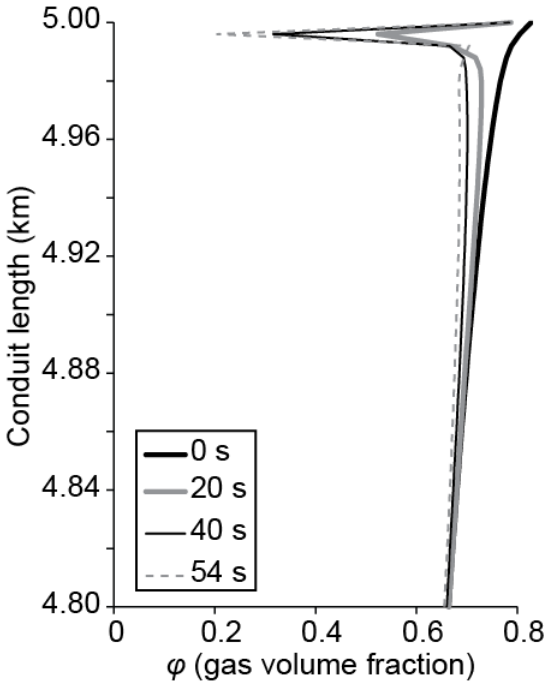

Figure 14: Gas volume fraction (φ) as a function of height in the conduit for the transient model with D_{Ni} and a single temperature. The condition at $t = 0$ s is the steady state and the later times shows the model response to a change of the permeability exponent in equation (2.6b) from 3.4 to 3.8 .

Changing the initial surface porosity coefficient, φ_0, within the range $0.1 - 0.7$ did not preclude plug formation at $D = 10^{-8}\ \mathrm{m}^2/\mathrm{s}$, hereby excluding any steady state from these initial conditions. Instead, to reach steady state with that D value, the model was initialized with $\varphi_0 = 0.25$ and $D = 10^{-13}\ \mathrm{m}^2/\mathrm{s}$ for the first 5'000 s. This allowed the porosity loss to be resorbed in a fashion similar to that depicted in Figure 13A. Then, D was changed to the target value of $10^{-8}\ \mathrm{m}^2/\mathrm{s}$ and the simulation was run until steady state was achieved. This procedure does not represent a natural scenario; its only purpose is to reach steady state at that D value. We applied the same initialization procedure to all the other cases with smaller D values ($\varphi_0 = 0.25$ and $D = 10^{-13}\ \mathrm{m}^2/\mathrm{s}$ until 5'000 s before setting D to the target value) and we obtained the same steady states as when setting D at the target value at $t = 0$ s. Also, varying φ_0 did not change the respective steady states reached.

The appearance of a low porosity region is not restricted to arbitrary initial conditions that are not compatible with the two-phase equation system (as in Figure 13). Magma permeability as deduced from eruptive products covers a broad range of values. In the permeability relationship (2.6b), we used the average exponent value of 3.4, but the full range of permeability from effusive products is covered by varying the exponent between 3 and 3.8 [Mueller et al., 2005]. Figure 14 shows a transient run with D_{Ni} that started from the steady state solution of Figure 13A at $t = 0$ s. The exponent of the permeability equation (2.6b) was changed from the original, average value of 3.4 to the largest value of 3.8 in 1 s. This abrupt change can represent a sudden increase of permeability near the surface, such as one due to local shear zone development or fracturing. At $\varphi = 0.6$, this change causes permeability to vary from 6×10^{-11} to $10^{-11}\ \mathrm{m}^2$. A shallow plug similar to those depicted in Figure 13 is created in ~ 1 min. Thus, an abrupt but moderate increase in the shallow permeability of the magma can cause plug formation.

6.2.1 Alternate outlet boundary condition

Similarly to the stationary case (Section 6.1.3), relaxing equal pressures at the outlet and setting instead $(p_g)_{|\Gamma_{\text{out}}} = p_{\text{top}}$ and $(p_l)_{|\Gamma_{\text{out}}}$ according to (5.8b) yields almost identical transient, variable temperature results on all variables (e.g., Figures 12–13) but p_l (cf. Figure 10). When this alternate boundary conditions is applied to the case of an overburden ($p_{\text{top}} = 2.5$ MPa), the change of the permeability exponent from 3.4 to 3.8 creates a plug directly centered on the outlet (i.e. φ has only one local maximum at shallow depth instead of two like in Figure 14. This behavior, however, is not due to the boundary condition; the same φ behavior occurs with equal outlet pressure and an overburden. This change in plug formation is instead caused by the fact that the overburden displaces the outlet position 100 m deeper than the case with $p_{\text{top}} = 0.1$ MPa, effectively localizing the outlet inside the plug of Figure 14 where $\varphi \to 0$.

The average pressure condition (5.8c) is very sensitive to velocity changes near the outlet because both p_g and p_l depend on the liquid velocity divergence (gradient in 1.5D). As p_l is given explicitly in (3.1i) and does not appear in the other equations of the system (3) when using (2.7) (see the implemented system (A.3)), negative p_l values do not impede the numerical resolution. This is not true for p_g, which is present in most equations, including in the R^{H_2O} expression (2.6d) under a square root. As a result, this condition is numerically unstable during the transient plug formation when $p_{\text{top}} = 0.1$ MPa because the plug causes a cycle of acceleration–deceleration near the outlet that yields $(p_g)_{|\Gamma_{\text{out}}} < 0$ during the iterative process. This precluded us to obtain transient solutions similar to those of Figures 12–13. To obtain steady-state solutions with $p_{\text{top}} = 0.1$ MPa, we ran the model with $p_{\text{top}} = 2.5$ MPa during the first 5000 s and then decreased p_{top} down to the target value of 0.1 MPa following a smooth step function over 2000 s to finally reach steady state at ~ 9000 s. The average pressure condition is thus unwieldy to study transient behavior with low outlet pressure and does not ensure strictly positive pressures.

7 Discussion

We presented a 1.5D model of volcanic conduit flow with two phases, gas and liquid, that conserves water mass and ensures total energy dissipation. We compared the outputs of this transient model to those of the well-established steady-state model of [Degruyter et al., 2012]. We assumed pure melt, which is restrictive assumption as most magmas contain crystals. If a two-phase framework is kept (i.e. solids are assumed to have the same velocity as the liquid), such solids mostly affect constitutive equations and have a limited effect on the structure of the transport equations presented herein. Crystals mostly change the rheology by inducing non-Newtonian behavior, and change magma permeability k. The reader is referred to [Melnik and Sparks, 2005] and [Costa et al., 2007a] for examples of how to take into account the effects of an additional solid phase on both the magma viscosity and density. Adopting a three-phase framework would be essential to predict solid-induced jamming and shear localization. A more immediate goal for future work than extending our model to three phases is to implement the 3D system (2.1) because it has the potential to address lateral distribution of pressure gradients, gas and heat loss at conduit walls, and to set a robust framework to study rheology changes due to shear localization.

The isothermal comparison between our model and that of [Degruyter et al., 2012] under conditions typical of an effusive eruption at an andesitic volcano suggests that strict equilibrium degassing is unreachable with a realistic water diffusion coefficient. Assuming equilibrium degassing recovers a realistic porosity evolution over most of the ascent, except near the surface where porosity is underestimated (Figure 1B). This is also the region where water balance is not respected (Figure 4). Overall, assuming equilibrium has a small influence on conduit flow pressure, ascent velocities, and thus on mass discharge rate.

We have shown in Part I, Section 5 [Narbona-Reina et al., 2024] that the relaxed system with $C_l = C_l^{\text{eq}}$, $T_g = T_l$, and $u_g = u_l$ can be expressed as three balances: conservation of the bulk mass, transport of C_T, and conservation

of the bulk momentum with a dual pressure gradient. This system has a Rayleigh-Plesset dilatancy that is a function of ratios of energy densities accounting for the work done by changing phases to maintain chemical equilibrium. Our results show a match between the relaxed and non-relaxed mass exchange rates of our transient model when $C_l = C_l^{\mathrm{eq}}$, but no match with the isothermal rate of the Degruyter model. This implies that the energy balance must be taken into account to accurately reproduce equilibrium degassing. In other words, the assumption $C_l = C_l^{\mathrm{eq}}$ cannot be made in an isothermal system.

Considering two pressures has two advantages. The first is that supersaturation pressures are readily available in the model outputs, which eases the assessment of whether a second nucleation event could be triggered (Figure 2C). Such events have been shown to occur during Vulcanian explosions [Formenti and Druitt, 2003], possibly triggering them [Burgisser et al., 2020]. The second advantage is that the transient behavior of the model is sensitive to the interplay between the gas/melt pressure difference and gas/melt separation (a.k.a. outgassing). Our results show that the shallow part of the conduit can be subject to localized porosity losses that can eventually create an impermeable plug (Figures 13-14). Plug formation occurs when φ is high enough to ensure permeable gas loss [Collombet, 2009], which causes p_g to decrease faster than p_l, yielding gas underpressure. The porosity reacts to that situation with a delay because Θ_V (and η_l) is large at shallow depth, but it eventually decreases in an attempt to equalize p_g and p_l. This porosity reduction is dampened by the slowing down of u_l in response to the increase of η_l, but in some of the conditions explored herein it is insufficient to avoid plug formation.

This observation opens an intriguing possibility; plug formation has traditionally been explained by degassing-induced crystallization (e.g., [Melnik and Sparks, 2005]; [Mason et al., 2006]; [Degruyter et al., 2012]). Our results suggest instead that plugs can be formed in crystal-free magmas. One difficulty that limits the usefulness of current conduit flow models is that mass flow rate strongly depends on conduit radius, which is a very poorly constrained variable (e.g., [Melnik and Sparks, 2005]). In that light, many complexities added by introducing, like in this work, a realistic diffusion and a strictly dissipative energy balance often have a very limited influence on the overall mass flow rate. Our steady-state solutions are no exception (Figure 5). The formation of a plug, however, can reduce or even stop mass flow rate, leading to a transient state bound to rapidly evolve. Further investigation will determine if some gas accumulates below the plug to foster its fragmentation. Note that, although our model does not feature fragmentation to better focus on effusive dynamics, it could be extended to include post-fragmentation flow following, for instance, [Mason et al., 2006] or [Degruyter et al., 2012]. We expect such investigation to be challenging numerically because (6.8) is not directly implemented in our numerical resolution. If it were, φ would remain $[0, 1]$ because the single form of the source term vanishes when $\varphi \to 0$, precluding any negative value of φ to occur. Instead, our implementation uses the dual form of the source term through (3.1i), which is not guaranteed to vanish when $\varphi \to 0$.

Our results show that releasing the isothermal assumption influences conduit flow by cooling due to gas expansion, which in turn increases melt viscosity and reduces the steady-state ascent velocity. This is consistent with the findings of other models with variable temperature ([Costa et al., 2007b]; [La Spina et al., 2017]). The model of [La Spina and de' Michieli Vitturi, 2012] has many similarities with ours, see Part I, Section 6 [Narbona-Reina et al., 2024]. One difference is that their exchange term does not involve diffusion. Under conditions similar to those we used herein (see Table 2), [La Spina et al., 2017] framed exsolution behavior by varying the relaxation time $\tau^{(d)}$ from 0.001 s (equilibrium mass transfer) to 1000 s (finite rate exsolution calibrated by reproducing experimental data of magma decompression) and to 10^{15} s (no mass transfer). Our results show that the relaxation time varies of one order of magnitude along the conduit length (0.03-0.5 s; Figure 9B). The model of [La Spina et al., 2017] can thus easily frame a particular diffusive behavior by assuming two constant $\tau^{(d)}$ values. Choosing the correct order of magnitude to explore, however, is challenging. The experimental set used by [La Spina et al., 2017] to determine 1000 s had D values of $\sim 10^{-11}\,\mathrm{m}^2/\mathrm{s}$ using (3.6), which is within the same range of D_{Ni} values as our runs. Considering that D_{Ni} is precise to a factor 1.6 [Ni and Zhang, 2008], this suggests that the calibration procedure used by [La Spina et al., 2017] overestimates $\tau^{(d)}$ by several orders of magnitude.

As shown in Part I, Section 6 [Narbona-Reina et al., 2024], our approach and that of [La Spina et al., 2017] differ. In our work, the gas phase is compressible and the liquid phase is incompressible with thus a constant density. Unlike a single fluid, however, this incompressibility does not imply a null divergence of the liquid velocity. Equations (2.4) and (6.6) both express the relationship between liquid pressure and $\mathrm{div}\ u_l$. [La Spina et al., 2017], on the other hand, consider two compressible components. The liquid phase has a pressure state law following:

$$(p_l)_{LS} = (c_{pl} - c_{vl})\rho_l T - \bar{p}_l$$

where c_{vl} is the heat capacity at constant volume and $\bar{p}_l$ quantifies the effects of the molecular attraction in the liquid phase at a reference pressure, density, and sound speed. As not all constraints on these two parameters are available in the literature, [La Spina et al., 2017] set them such that the density all along the conduit is close to a target, constant value. Following the same reasoning for $(p_l)_{LS}$ with p_l as the target value, we set $c_{vl} = 30$ J/kg/K and $\bar{p}_l = 2.6 \times 10^9$ Pa to recalculate $(p_l)_{LS}$ from our transient model outputs.

Results show that both liquid pressures share a similar trend over most of the ascent because the ratio $p_l/(p_l)_{LS}$ varies between 0.8 and 1.2 from the inlet to 4950 m, regardless of whether outlet pressures are equal or not in our transient model. Over the last 50 m of the ascent, however, $(p_l)_{LS}$ drops abruptly to reach the negative value of -63 MPa for equal outlet pressures. When the outlet liquid pressure is governed by (5.8b), $(p_l)_{|\Gamma_{\mathrm{out}}} = -5$ MPa and $(p_l)_{LS}=$ -65 MPa. When an overburden is present, $(p_l)_{LS} = -28$ MPa, regardless of whether outlet pressures are both equal to 2.5 MPa, or $(p_g)_{|\Gamma_{\mathrm{out}}} = 2.5$ MPa and $(p_l)_{|\Gamma_{\mathrm{out}}} = 1.9$ MPa. Conversely, we expect that p_l given by equation (2.4) recalculated from La Spina model outputs would also yield unrealistic values. This suggests that the two approaches (assuming the liquid to be either incompressible or a stiff gas) are not compatible with each other in regions of large liquid acceleration. In other words, we anticipate that this divergence of behavior will systematically occur in regions where $\mathrm{div}\ u_l$ is large.

[Costa et al., 2007b] propose a scaling analysis of the effects of shear heating that is based on the Graetz number, which, using the convention of the scaling in Part I, Section 4 [Narbona-Reina et al., 2024], corresponds to:

$$\mathrm{Gz} = \mathrm{Pe}_b \frac{r_c}{H} \qquad \text{with} \qquad L_0 = r_c.$$

where Pe_b is the Peclet number based on bulk properties (e.g., $\kappa_b = \varphi\kappa_g + (1-\varphi)\kappa_l$). Assuming $\varphi = 0.1$ to estimate these bulk properties, the Graetz number of our run is $\sim 10^5$, which corresponds to a partially developed flow where the heat conduction from the colder wall affects a narrow layer of magma near the conduit walls. The Nahme number, Na, is the ratio between the temperature at which rheology changes and the typical temperature scale:

$$\mathrm{Na} = \frac{u_{l0}^2}{\kappa_b}(\partial_{T_l}\eta_l)_{T_{l0}}$$

In our runs, Na is ~ 20, which indicates that viscous effects cannot be neglected, but that they are subordinate to potential heat loss at the conduit walls because $\mathrm{Na}/\sqrt{\mathrm{Gz}} \ll 0.2$. Our results indicate that the cooling due to gas expansion at shallow level exceeds shear heating effects (Figure 8). The scaling proposed by [Costa et al., 2007b] is thus useful to take first-order decisions about the inclusion of shear heating. Because our model considers two temperatures and gas-liquid separation affects the energy balance, we suggest combining this scaling with our other scaling quantities in Part I, Section 4 [Narbona-Reina et al., 2024] to refine the analysis before dropping energy dissipation terms.

We used the steady-state solution of the single temperature model with D_{Ni} to establish under which conditions some physical processes could be neglected so that the mass discharge rate of the resulting simplified model (6.9) remains within 10 % of that of the full model. Figure 15 shows two synthetic regime diagrams highlighting when the

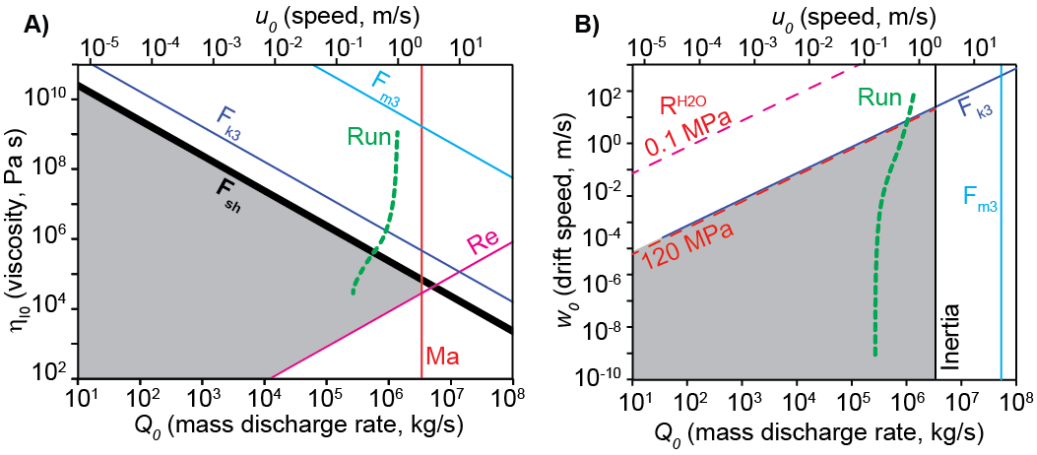

Figure 15: Regime diagrams mapping the parameter space where the simplified model (6.9) is valid. Green curves mark the transient run with D_{Ni} and a single temperature. A) Liquid viscosity (η_{l0}) as a function of mass discharge rate (Q_0) and ascent rate (u_0). The gray area indicates where shear heating (F_{sh}) and liquid inertia (Re and Ma at $p_0 = 0.1$ MPa) can be neglected and where Darcy's law (F_{m3} and F_{k3} at $w_0/(k_0 p_0) = 1$) is valid. B) Drift speed (w_0) as a function of Q_0 and u_0. The gray area indicates where mass exchange (R^{H_2O} at two pressures), liquid inertia (Ma at 0.1 MPa and Re at $\eta_{l0} = 3 \times 10^4$ Pa s) can be neglected and where Darcy's law (F_{m3} and F_{k3} at $p_0 k_0 \eta_{l0} = 1.2 \times 10^6$ with that product maximized by taking $p_0 = 120$ MPa, $k_0 = 10^{-10}$ m^2, and $\eta_{l0} = 10^8$ Pa s) is valid.

simplifications considered in Section 6.1.4 are valid. Each scaling variable was either maximized or minimized to obtain the largest possible parameter space where these simplifications hold. Although these diagrams cover a wide range of mass discharge rate characteristic of effusive eruptions, they are based on keeping many variables constant (e.g., conduit geometry, Table 3). The regime boundaries are sensitive to changes in these variables (such as conduit length, [Slezin, 2003]), so the situation portrayed by Figure 15 cannot be freely extrapolated beyond the bounds listed in Table 3.

Constraining liquid viscosity and mass discharge rate (or ascent rate) has practical applications as these variables can be measured or estimated during an eruption. For instance, eruptions with ascent rates inferior to $10^{-1} - 10^{-3}$ m/s ($2 \times 10^3 - 2 \times 10^5$ kg/s with a 30-m conduit) are generally effusive [Cassidy et al., 2018]. Figure 15A suggests that the effusive regime can be approximated by the simplified system (6.9). It also suggests pairing of physical simplifications; if shear heating can be neglected then obtaining the gas velocity from Darcy's equation is also valid. Describing regime boundaries for the applicability of Darcy's law is important as this is a popular assumption (e.g., [Melnik and Sparks, 2005]; [Costa et al., 2007a]). Constraining the drift speed (Figure 15B) has implications that are harder to grasp because field estimates of the velocity difference between gas and liquid can only be obtained at the vent. We can nevertheless expect that the simplified system can capture flow conditions when $w_0 \leq 10^{-6} - 10^{-4}$ m/s, which is likely to occur at high pressure where porosity is low and $k \sim 10^{-13} - 10^{-15}$ m^2.

That the pressure difference allowed by the viscous relaxation is a key to plug formation is a counter-intuitive result. [Fowler and Robinson, 2018], for instance, noted that *"the average gas and liquid pressures are generally different,* [including] *terms representing bulk viscosity and bubble collapse as well as surface tension. In an earlier draft of this paper, many such terms were included, and then it was shown through scaling arguments that they were all small in comparison to the pressure difference along the conduit, so we will take the pressures to be equal."* Together with our scaling in Part I, Section 4 [Narbona-Reina et al., 2024], this highlights that scaling is a difficult task when there is more than a single length scale involved and when scaled variables (such as p_g) span several orders of magnitude over the domain length.

8 Conclusion

We presented a 3D model of volcanic conduit flow with two phases, gas and liquid, that conserves water mass and ensures energy dissipation. Water mass conservation is ensured by including an exchange term based on a first-order Taylor development of the diffusion flux of dissolved water from the melt to the gas bubble at the interface. It has the sought properties of tending to 0 at vanishing porosity and to infinity when $\varphi \to 1$. Results shows that it yields similar values as the exchange term proposed by [Lyakhovsky et al., 1996] based on the concentration gradient at the bubble interface under quasi-static diffusion.

We then proposed a 1.5D simplification of this 3D model. Three types of terms cause difficulties in its numerical implementation. The first type of issue is the presence of p_l in both the liquid momentum and the Rayleigh-Plesset equation. The second issue is the temperature coupling in both liquid and gas temperature equation through the heat exchange factor γ. The third is the presence of both gas pressure and gas temperature derivatives in the gas temperature equation. We proposed a rewritten system that alleviates these issues and yields stable numerical solutions.

We compared the outputs of our 1.5D transient model to those of the steady-state, equilibrium degassing, isothermal model of [Degruyter et al., 2012] under conditions typical of an effusive eruption at an andesitic volcano. This comparison suggests that strict equilibrium degassing is unreachable with a realistic water diffusion coefficient. However, assuming equilibrium degassing at ascent rates $<$0.4 m/s at the inlet recovers a realistic porosity evolution over most of the ascent, except near the surface where porosity is underestimated and water mass balance is not respected. Overall, assuming equilibrium degassing has a small influence on conduit flow pressure, ascent velocities, and thus on mass discharge rate. In contrast, releasing the isothermal assumption influences conduit flow by cooling due to gas expansion, which in turn increases melt viscosity and reduces the steady-state ascent velocity. This is consistent with previous findings [La Spina et al., 2017].

We proposed a simplified system using Darcy's law and omitting shear heating, the inertial and mass exchange terms in the liquid momentum equation, and mass exchange in the dilatancy equation. This minimal system system is not dissipative but approximates the steady-state mass discharge rate of the full system within 10%. A regime diagram valid under a limited set of conditions indicates that this minimal system could capture the ascent dynamics of the effusive regime. Interestingly, the two novel aspects of the full model, diffusive degassing and heat balance, cannot be neglected.

It is not trivial to initialize the transient model with conditions that are compatible with the two-phase equation system. We found that imposing equal pressures at both conduit ends (rather than inlet velocities or outlet unequal pressures) and starting from the hydrostatic pressure distribution of a bubble-free magma with a linear porosity distribution and a water content at saturation yield good results in most cases. The transient solutions at the transfer time of $H/(u_l)_{|\Gamma_{\text{in}}}$ offer a good representation of steady state because it is the time taken to advect C_l from depth to surface.

In some cases with high diffusion coefficients ($> 10^{-11}\,\mathrm{m}^2/\mathrm{s}$ under the conditions explored herein), a shallow region where φ, u_l, and u_g tend towards zero develops initially, possibly blocking an eventual steady state. This local porosity loss also occurs when a steady-state solution is subjected to a change in shallow permeability. Such case, which is likely to happen shallowly as a result of dome growth processes, leads to a porosity loss that features many characteristics of a plug developing prior to a Vulcanian eruption. Our preliminary results show that plug formation is fostered when the flow conditions yield $\varphi \sim 0.5$ and $p_g < p_l$ because of gas loss towards the outlet. Further investigation will determine if some gas accumulates below the plug to foster its fragmentation. This type of dynamics can only be addressed by a two-pressure model that ensures water mass conservation and explicitly includes water diffusivity as a model parameter.

A Computation details

This Appendix contains details of how the transient model is implemented in the finite element commercial software *COMSOL Multiphysics v5.6*. For user-friendliness, we kept within the Appendix notations consistent with the software documentation. The spatial variable is the height along the conduit that we denoted by z in the main text. Nevertheless, for 1D problems in *COMSOL Multiphysics*, the independent variable is denoted by x. To avoid confusion in the computational code notation that is used in this Appendix, we assume the notation x for the independent variable, keeping in mind that, when referring to the main text, $z \equiv x$. Also, derivatives in this software are calculated as $d(f, x)$ for any function f.

We use the "Coefficient Form PDE" module of the software, which implements a general equation of the form :

$$e_a \partial_{t^2}^2 U + d_a \partial_t U + \mathrm{div}(-c\nabla U - \alpha U + \gamma) + \beta \cdot \nabla U + aU = f \tag{A.1}$$

where U is the vector of unknowns and e_a, d_a are the mass coefficients, c is the diffusion coefficient, α the conservative flux convection coefficient, γ the conservative flux source, β the convection coefficient, a the absorption coefficient and f the source term. The PDE module automatically converts the above equations written in coefficient form to the weak form, and that weak form is solved by the software using the finite element method. The Dirichlet type boundary conditions are introduced using the corresponding module "Dirichlet Boundary Condition" and the flux conditions through the "Flux/source" module that has the general expression:

$$-n \cdot (-c\nabla U - \alpha U + \gamma) = g - qU, \tag{A.2}$$

where n is the outward vector normal to the boundary. Both boundary condition types are also converted into their weak from counterparts by *COMSOL*.

A.1 Implementation of the transient model

In order to write the computational system, the 9 unknowns of the differential system (3.1a), (3.1b), (3.1c), (3.1d), (3.1e), (3.1h), (3.1i), and the 1.5D version of (2.12) and (2.11) are denoted as follows:

$$U = (\texttt{Clphi}, \texttt{rholphi}, \texttt{rhogphi}, u_l, T_l, p_g, u_g, T_g, p_l)^t$$

where

$$\texttt{Clphi} = \rho_l(1-\varphi)(1-C_l), \quad \texttt{rholphi} = \rho_l(1-\varphi), \quad \texttt{rhogphi} = \rho_g\varphi,$$

are the conservative variables. The primitive variables are obtained as

$$\varphi = 1 - \frac{\texttt{rholphi}}{\rho_l}; \quad C_l = 1 - \frac{\texttt{Clphi}}{\texttt{rholphi}}; \quad \rho_g = \frac{\texttt{rhogphi}}{\varphi}.$$

The momentum equations were coded in non-conservative form because it is the default form proposed in Comsol, because it is more amenable to implement boundary conditions. Most of the runs presented herein are performed with considering identical gas and liquid temperatures. We implemented an unified code whether $T_g = T_l$ or not. For clarity, we write the system with the primitive variables and in the same order as in the vector of unknown U,

$$\partial_t((1-\varphi)\rho_l(1-C_l)) + \partial_x((1-\varphi)\rho_l(1-C_l)u_l) = 0 \tag{A.3a}$$

$$\partial_t((1-\varphi)\rho_l) + \partial_x((1-\varphi)\rho_l u_l) = -R^{H_2O} \tag{A.3b}$$

$$\partial_t(\varphi\rho_g) + \partial_x(\varphi\rho_g u_g) = R^{H_2O} \tag{A.3c}$$

$$\begin{aligned}(1-\varphi)\rho_l(\partial_t u_l + u_l\partial_x u_l) + \partial_x\left((1-\varphi)p_g - \frac{R^{H_2O}}{\rho_l\varphi\chi} - \frac{4(1-\varphi)\eta_l}{3\varphi}\partial_x u_l\right) + \tilde{\beta}u_l \\ - p_g\partial_x(1-\varphi) - K_d\,\varphi(1-\varphi)(u_g-u_l) = (1-\varphi)\rho_l g - \frac{u_g-u_l}{2}R^{H_2O}\end{aligned} \tag{A.3d}$$

$$\begin{aligned}c_{pl}(1-\varphi)\rho_l\left(\partial_t T_l + u_l\partial_x T_l\right) + (c_{pg}-c_0)\varphi\rho_g\Big(\partial_t T_g + u_g\partial_x T_g\Big) + p_g\partial_x(\varphi u_g + (1-\varphi)u_l) \\ + ((c_{pg}-c_0)T_g - c_{pl}T_l)R^{H_2O} = -\frac{R^{H_2O}}{\rho_l\varphi\chi}\left(\partial_x u_l + \frac{R^{H_2O}}{\rho_l(1-\varphi)}\right) + \tilde{\beta}u_l^2.\end{aligned} \tag{A.3e}$$

$$p_g = c_0\rho_g T_g \tag{A.3f}$$

$$\varphi\rho_g(\partial_t u_g + u_g\partial_x u_g) + \partial_x(\varphi p_g) - p_g\partial_x\varphi + K_d\,\varphi(1-\varphi)(u_g-u_l) = \varphi\rho_g g - \frac{u_g-u_l}{2}R^{H_2O} \tag{A.3g}$$

$$B_T\left((c_{pg}-c_0)\varphi\rho_g(\partial_t T_g + u_g\partial_x T_g) + p_g\partial_x\Big(\varphi u_g + (1-\varphi)u_l\Big)\right) = \gamma(T_g - T_l) - B_T\Big(\frac{p_g}{\rho_l} + (c_{pg}-c_0)T_g\Big)R^{H_2O} \tag{A.3h}$$

$$p_l = p_g - \frac{1}{\varphi\chi}\left(\partial_x u_l + \frac{R^{H_2O}}{\rho_l(1-\varphi)}\right) \tag{A.3i}$$

As (A.3e) is the 1.5D equivalent of (2.13) when $T_g = T_l$, we introduced the binary variable B_T to easily switch to a single-temperature:

$$B_T = \begin{cases} 1 & \text{when } T_g \neq T_l \\ 0 & \text{when } T_g = T_l \end{cases}$$

We also implemented a version of the code with $T_g = T_l = T$ and without (A.3h) to reduce the size of U and the associated resolution matrices in (A.1) for computational efficiency.

Coefficients for (A.1) are as follow:

- $e_a = 0$,
- d_a (mass coefficient) is a 9×9 matrix with non-zero values $(d_a)_{11} = 1, (d_a)_{22} = 1, (d_a)_{33} = 1, (d_a)_{44} = \texttt{rholphi}, (d_a)_{55} = c_{pl}\texttt{rholphi}, (d_a)_{58} = (c_{pg}-c_0)\texttt{rhogphi}, (d_a)_{77} = \texttt{rhogphi}, (d_a)_{88} = B_T(c_{pg}-c_0)\texttt{rhogphi}$,
- c (diffusion coefficient) is a 9×9 diagonal matrix with just one non-zero value $c_{44} = \dfrac{4(1-\varphi)\eta_l}{3\varphi}$
- α (conservative flux convection coefficient) is a 9×9 diagonal matrix with elements in the diagonal $(-u_l, -u_l, -u_g, 0, 0, 0, 0, 0, 0)$,
- γ (conservative flux source) is a vector with non-zero values $\gamma_4 = (1-\varphi)p_g - \dfrac{R^{H_2O}}{\rho_l\chi\varphi}$, $\gamma_7 = \varphi p_g$

- β (convection coefficient) is a 9×9 matrix with non-zero values $\beta_{44} = \texttt{rholphi}\, u_l$, $\beta_{55} = c_{pl}\texttt{rholphi}\, u_l$, $\beta_{58} = (c_{pg} - c_0)\texttt{rhogphi}\, u_g$, $\beta_{77} = \texttt{rhogphi}\, u_g$, $\beta_{88} = B_T(c_{pg} - c_0)\texttt{rhogphi}\, u_g$,

- a (absorption coefficient) is a 9×9 matrix with the following elements
  $a_{44} = K_d\,\varphi(1-\varphi) + \tilde{\beta}$, $a_{46} = d(\varphi, x)$, $a_{47} = -K_d\,\varphi(1-\varphi)$,
  $a_{55} = -c_{pl}R^{H_2O}$, $a_{56} = d(\varphi u_g + (1-\varphi)u_l, x)$, $a_{58} = (c_{pg} - c_0)R^{H_2O}$
  $a_{66} = 1$,
  $a_{74} = a_{47}$, $a_{76} = -d(\varphi, x)$, $a_{77} = -a_{47}$,
  $a_{86} = B_T\left(d(\varphi u_g + (1-\varphi)u_l, x) + \frac{R^{H_2O}}{\rho_l}\right)$, $a_{88} = -\gamma B_T(c_{pg} - c_0)R^{H_2O}$,
  $a_{96} = -1$, $a_{99} = 1$,

- f (source term) is a vector defined by
  $f_1 = 0$,
  $f_2 = -R^{H_2O}$,
  $f_3 = R^{H_2O}$,
  $f_4 = \texttt{rholphi}\; g - \frac{u_g - u_l}{2}R^{H_2O}$,
  $f_5 = -\frac{R^{H_2O}}{\rho_l \chi \varphi}(d(u_l, x) + \frac{R^{H_2O}}{\texttt{rholphi}}) + \tilde{\beta}u_l^2$,
  $f_6 = c_0\rho_g T_g$,
  $f_7 = \texttt{rhogphi}\; g - \frac{u_g - u_l}{2}R^{H_2O}$,
  $f_8 = \gamma T_l$,
  $f_9 = -\frac{1}{\chi\varphi}\left(d(u_l, x) + \frac{R^{H_2O}}{\texttt{rholphi}}\right)$.

Initial conditions are coded following (5.5) for the conservative variables, so

$$\begin{aligned} &(\texttt{Clphi})_{|t=0} = \rho_l(1-\varphi^i)(1-C_l^i); \qquad (\texttt{rholphi})_{|t=0} = \rho_l(1-\varphi^i); \qquad (\texttt{rhogphi})_{|t=0} = \varphi^i p_g^i/(c_0 T_{\text{in}}); \\ &(u_l)_{|t=0} = (u_g)_{|t=0} = u^i; \qquad (p_g)_{|t=0} = (p_l)_{|t=0} = p_g^i; \qquad (T_g)_{|t=0} = (T_l)_{|t=0} = T_{\text{in}}. \end{aligned} \tag{A.4}$$

The Dirichlet boundary conditions at the inlet follow the values defined in (5.7):

$$\begin{aligned} &(p_l)_{|\Gamma_{\text{in}}} = (p_g)_{|\Gamma_{\text{in}}} = p_{\text{in}}; \quad (T_l)_{|\Gamma_{\text{in}}} = (T_g)_{|\Gamma_{\text{in}}} = T_{\text{in}}; \quad (\texttt{rhogphi})_{|\Gamma_{\text{in}}} = \varphi_{\text{in}} p_{\text{in}}/(c_0 T_{\text{in}}); \\ &(\texttt{Clphi})_{|\Gamma_{\text{in}}} = \rho_l(1-\varphi_{\text{in}})(1-(C_l)_{\text{in}}); \quad (\texttt{rholphi})_{|\Gamma_{\text{in}}} = \rho_l(1-\varphi_{\text{in}}). \end{aligned} \tag{A.5}$$

The Neumann condition (5.9) is coded using the "Flux/source" module through the general form equation (A.2). Notice that for equations with non-zero values of any of the coefficients appearing in this equation, c, α, γ, it forces no-flux contribution at the inlet. In our system this affects variables in positions 1,2,3,4,7. Removing this forcing is done by specifying the following coefficients:

- g, vector with components

$$\begin{aligned} g_1 &= -u_l\; \texttt{Clphi}\; n_x, \\ g_2 &= -u_l\; \texttt{rholphi}\; n_x, \\ g_3 &= -u_g\; \texttt{rhogphi}\; n_x, \\ g_4 &= -(1-\varphi)p_g\; n_x, \\ g_5 &= 0, \\ g_6 &= 0, \\ g_7 &= -\varphi p_g n_x, \\ g_8 &= 0, \\ g_9 &= 0; \end{aligned}$$

- $q = 0$.

In other words, all the non-zero terms in $g_{1,2,3,7}$ simply make free conditions for the corresponding variables ($0 = 0$) due to the pre-programmed presence of conservative flux α, γ and diffusion c.

The boundary conditions at the outlet for pressures, (5.8a), are imposed as Dirichlet conditions:

$$(p_l)_{|\Gamma_{\text{out}}} = (p_g)_{|\Gamma_{\text{out}}} = p_{\text{top}}.$$

The additional numerical condition (5.9) is coded in the same way as the inlet boundary and it is combined with the alternative conditions for an hypothetical entering flow situation in (5.8d). It is imposed through the coefficients:

- g, vector with components

$$\begin{aligned}
g_1 &= -u_l \ \texttt{Clphi} \ n_x - (\texttt{Clphi} - \texttt{Clphi}_{|\Gamma_{\text{out}}})(u_l n_x < 0),\\
g_2 &= -u_l \ \texttt{rholphi} \ n_x - (\texttt{rholphi} - \texttt{rholphi}_{|\Gamma_{\text{out}}})(u_l n_x < 0),\\
g_3 &= -u_g \ \texttt{rhogphi} \ n_x - (\texttt{rhogphi} - \texttt{rhogphi}_{|\Gamma_{\text{out}}})(u_g n_x < 0),\\
g_4 &= -(1-\varphi) p_g \ n_x,\\
g_5 &= -(T_l - (T_l)_{|\Gamma_{\text{out}}})(u_l n_x < 0),\\
g_6 &= 0,\\
g_7 &= -\varphi p_g \ n_x,\\
g_8 &= -(T_g - (T_g)_{|\Gamma_{\text{out}}})(u_g n_x < 0),\\
g_9 &= 0;
\end{aligned}$$

- $q = 0$,

  where the variables with indices $|\Gamma_{\text{out}}$ are set to their initial values evaluated at $x = H$.

  When the $(p_l)_{|\Gamma_{\text{out}}} \neq (p_g)_{|\Gamma_{\text{out}}}$ condition is coded, the Dirichlet condition becomes:

$$(p_g)_{|\Gamma_{\text{out}}} = p_{\text{top}} \qquad (p_l)_{|\Gamma_{\text{out}}} = p_{\text{top}} - \frac{1}{\chi\varphi}(\text{dtang}(u_l, x) + (R^{H_2O})_{|\Gamma_{\text{out}}}/\texttt{rholphi})$$

  where

$$(R^{H_2O})_{|\Gamma_{\text{out}}} = 3^{1/3}\Big(4\pi N \varphi(1-\varphi)\Big)^{2/3} D \frac{C_l - k_h\sqrt{p_{\text{top}}}}{\rho_l(1-\varphi^{1/3})}$$

and $\text{dtang}(u_l, x)$ is an operator that calculates the derivative of u_l in the x-direction (for the 1D case) at the boundary where the evaluation takes place. This formulation takes advantage of the COMSOL setup that Dirichlet conditions are set in an unidirectional fashion, applying right-hand-side terms on the left-hand side term (here $(p_l)_{|\Gamma_{\text{out}}}$) but not on any variables appearing in the right-hand-side of the condition. D is evaluated at p_{top} if D_{Ni} is used. The component g_4 above is replaced by:

$$g_4 = \Big((1-\varphi)p_g + R^{H_2O}/(\rho_l \chi\varphi) + (1-\varphi)d(u_l, x)/(\varphi\chi)\Big)n_x.$$

A.2 Numerical method

The sensitivity of solutions to domain discretization was tested at uniform intervals of 8, 4, and 1 m over the 5000-m long domain. Solutions were independent of interval sizes for the two smaller values, so 4-m intervals were chosen for all runs except the one featured in Figure 14, where 1-m intervals were used to better resolve the low-porosity region. We used cubic Hermite elements for the discretization of variables in the system, thus ensuring the continuity of the first derivatives at the nodes. The PARDISO solver is used with the default options, a relative tolerance on the residuals of 10^{-3} to 2×10^{-3}, and an absolute tolerance of 10^{-3}. Variables were scaled according to their initial values. In transient runs, time stepping was done using the BDF algorithm with a maximum time step of 0.1 s. Stored time steps were those obtained from the solver to avoid interpolation inaccuracies.

B Energy of the simplified system

Following the same steps than in Section 2.5 of [Narbona-Reina et al., 2024], we find formally (when no boundary conditions are applied) the following energy balance for the simplified system (6.9):

$$\begin{aligned}
&\partial_t\left(\frac{1}{2}(1-\varphi)\rho_l u_l^2 + gz(1-\varphi)\rho_l + c_{pn}T\right) + \partial_z\left((1-\varphi)p_l u_l + gz(1-\varphi)\rho_l u_l + c_{pm}Tu_T\right)\\
&\quad = -\varphi(1-\varphi)\chi(p_g-p_l)^2 - K_d\varphi(1-\varphi)(u_g-u_l)^2 - \tilde{\beta}u_l^2\\
&\qquad - gzR^{H_2O} + \frac{1}{2}u_l^2\Big(\partial_z((1-\varphi)\rho_l u_l) + R^{H_2O}\Big) - (p_g-p_l)\frac{R^{H_2O}}{\rho_l}
\end{aligned} \tag{B.1}$$

The first two terms on the right-hand side are the dissipative contributions also present in the energy of the complete model. The term $\tilde{\beta}u_l^2$ stems from neglecting the shear heating in the temperature equation. The gravity term gzR^{H_2O} is a consequence of replacing the gas momentum equation by Darcy's law. The term $\frac{1}{2}u_l^2\Big(\partial_z((1-\varphi)\rho_l u_l) + R^{H_2O}\Big)$ is related to both Darcy's law and the neglected inertial term in the liquid momentum equation. Finally, the term $R^{H_2O}(p_g-p_l)/\rho_l$ stems from neglecting mass exchange in the dilatancy equation (6.6).

Is the simplified system dissipative? The three first terms on the right-hand side of (B.1) yield a dissipative total contribution. Note that the term $|u_l|^2(\partial_z((1-\varphi)\rho_l u_l)/2 + R^{H_2O}$ on the right-hand side of (B.1) comes from the fact that in (6.9) we have neglected the inertial quantity $\partial_z((1-\varphi)u_l\rho_l)$. If we also suppress the term $\partial_t((1-\varphi)\rho_l u_l)$, then $|u_l|^2(\partial_z((1-\varphi)\rho_l u_l)/2 + R^{H_2O}$ does not appear in (B.1) but we lose also the quantity $\partial_t((1-\varphi)\rho_l u_l^2)/2$ on the left-hand side of (B.1). If the time derivative on $(1-\varphi)\rho_l u_l$ is also suppressed, then the time dependency of u_l is given through the non-stationary equations on φ and T. This is what is called a semi-stationary system. Assuming such a semi-stationary system, the last quantity with an undefined sign is $(p_g - (p_l - \rho_l gz))R^{H_2O}$. Recall that R^{H_20} has the same sign that $C_l - k_h\sqrt{p_g}$. Therefore we have the following cases:

- $(p_g - (p_l - \rho_l gz))R^{H_2O} \geq 0$ (dissipative case) if
  - $C_l \geq K_h\sqrt{p_g}$ and $p_g \geq p_l - \rho_l gz$
  - or $C_l \leq K_h\sqrt{p_g}$ and $p_g \leq p_l - \rho_l gz$
- $(p_g - (p_l - \rho_l gz))R^{H_2O} \leq 0$ (non-dissipative, unstable case) if
  - $C_l \geq K_h\sqrt{p_g}$ and $p_g \leq p_l - \rho_l gz$
  - or $C_l \leq K_h\sqrt{p_g}$ and $p_g \geq p_l - \rho_l gz$

Acknowledgements

The authors want to thank the University Savoie Mont Blanc and the CNRS for various financial supports (such as MODTRANS, TelluS-INSMI-MI projects and invited positions in Chambéry) during the several enjoyable years it took to build this long triptych. This work was partially supported by the Agence Nationale pour la Recherche grant ANR-19-CE31-0007 and ANR-18-CE40-0027. G. Narbona-Reina wants to thank the grant REC-B-22376-1 and REC-B-22376-2 funded by MICIU/AEI/ 10.13039/501100011033 and by the "European Union NextGenerationEU/PRTR", and the National Spanish grant PID2022-137637NB-C22 funded by MCIN/AEI/10.13039/501100011033 and by "ERDF A way of making Europe", for financial support. We also thank C. Acary-Robert for discussions several years ago at the beginning of this multi-disciplinary project.

References

[Bresch et al., 2024] Bresch, D., Narbona-Reina, G., Burgisser, A., and Collombet, M. (2024). Mathematical topics in compressible flows from mono-phase systems to two-phase systems. Submitted.

[Burgisser et al., 2020] Burgisser, A., Arbaret, L., Martel, C., Forien, M., and Colombier, M. (2020). The role of oxides in the shallow vesiculation of ascending magmas. *Journal of Volcanology and Geothermal Research*, 406:107072.

[Burgisser et al., 2017] Burgisser, A., Chevalier, L., Gardner, J. E., and Castro, J. M. (2017). The percolation threshold and permeability evolution of ascending magmas. *Earth and Planetary Science Letters*, 470:37–47.

[Burgisser and Gardner, 2004] Burgisser, A. and Gardner, J. E. (2004). Experimental constraints on degassing and permeability in volcanic conduit flow. *Bulletin of Volcanology*, 67(1):42–56.

[Cassidy et al., 2018] Cassidy, M., Manga, M., Cashman, K., and Bachmann, O. (2018). Controls on explosive-effusive volcanic eruption styles. *Nature Communications*, 9(1):2839.

[Castro et al., 2012] Castro, J. M., Burgisser, A., Schipper, C. I., and Mancini, S. (2012). Mechanisms of bubble coalescence in silicic magmas. *Bulletin of Volcanology*, 74(10):2339–2352.

[Choudhary et al., 2016] Choudhary, A., Roy, C. J., Luke, E. A., and Veluri, S. P. (2016). Code verification of boundary conditions for compressible and incompressible computational fluid dynamics codes. *Computers and Fluids*, 126:153–169.

[Collier and Neuberg, 2006] Collier, L. and Neuberg, J. (2006). Incorporating seismic observations into 2d conduit flow modeling. *Journal of Volcanology and Geothermal Research*, 152(3):331–346.

[Collombet, 2009] Collombet, M. (2009). Two-dimensional gas loss for silicic magma flows: Toward more realistic numerical models. *Geophysical Journal International*, 177(1):309–318.

[Costa et al., 2007a] Costa, A., Melnik, O., and Sparks, R. (2007a). Controls of conduit geometry and wallrock elasticity on lava dome eruptions. *Earth and Planetary Science Letters*, 260:131–151.

[Costa et al., 2007b] Costa, A., Melnik, O., and Vedeneeva, E. (2007b). Thermal effects during magma ascent in conduits. *Journal of Geophysical Research: Solid Earth*, 112(B12).

[Costa et al., 2009] Costa, A., Sparks, R., Macedonio, G., and Melnik, O. (2009). Effects of wall-rock elasticity on magma flow in dykes during explosive eruptions. *Earth and Planetary Science Letters*, 288(3):455–462.

[Coumans et al., 2020] Coumans, J. P., Llewellin, E. W., Wadsworth, F. B., Humphreys, M. C. S., Mathias, S. A., Yelverton, B. M., and Gardner, J. E. (2020). An experimentally validated numerical model for bubble growth in magma. *Journal of Volcanology and Geothermal Research*, 402:107002.

[Crozier et al., 2022] Crozier, J., Tramontano, S., Forte, P., Oliva, S. J. C., Gonnermann, H. M., Lev, E., Manga, M., Myers, M., Rader, E., Ruprecht, P., Tuffen, H., Paisley, R., Houghton, B. F., Shea, T., Schipper, C. I., and Castro, J. M. (2022). Outgassing through magmatic fractures enables effusive eruption of silicic magma. *Journal of Volcanology and Geothermal Research*, 430:107617.

[Dartevelle and Valentine, 2007] Dartevelle, S. and Valentine, G. A. (2007). Transient multiphase processes during the explosive eruption of basalt through a geothermal borehole (námafjall, iceland, 1977) and implications for natural volcanic flows. *Earth and Planetary Science Letters*, 262(3):363–384.

[Degruyter et al., 2012] Degruyter, W., Bachmann, O., Burgisser, A., and Manga, M. (2012). The effects of outgassing on the transition between effusive and explosive silicic eruptions. *Earth and Planetary Science Letters*, 349-350:161–170.

[Dufek and Bergantz, 2005] Dufek, J. and Bergantz, G. W. (2005). Lower Crustal Magma Genesis and Preservation: a Stochastic Framework for the Evaluation of Basalt,ÄìCrust Interaction. *Journal of Petrology*, 46(11):2167–2195.

[Forestier-Coste et al., 2012] Forestier-Coste, L., Mancini, S., Burgisser, A., and James, F. (2012). Numerical resolution of a mono-disperse model of bubble growth in magmas. *Applied Mathematical Modelling*, 36(12):5936 – 5951.

[Formenti and Druitt, 2003] Formenti, Y. and Druitt, T. (2003). Vesicle connectivity in pyroclasts and implications for the fluidisation of fountain-collapse pyroclastic flows, Montserrat (West Indies). *Earth and Planetary Science Letters*, 214(3-4):561–574.

[Fowler and Robinson, 2018] Fowler, A. and Robinson, M. (2018). Counter-current convection in a volcanic conduit. *Journal of Volcanology and Geothermal Research*, 356:141–162.

[Gardner and Denis, 2004] Gardner, J. E. and Denis, M.-H. (2004). Heterogeneous bubble nucleation on fe-ti oxide crystals in high-silica rhyolitic melts. *Geochimica et Cosmochimica Acta*, 68(17):3587–3597.

[Giordano et al., 2008] Giordano, D., Russell, J., and Dingwell, D. (2008). Viscosity of magmatic liquids: A model. *Earth and Planetary Science Letters*, 271:123–134.

[Gonnermann and Manga, 2007] Gonnermann, H. and Manga, M. (2007). The fluid mechanics inside a volcano. *Annual Review of Fluid Mechanics*, 39:321–356.

[González-Mellado and De la Cruz-Reyna, 2008] González-Mellado, A. O. and De la Cruz-Reyna, S. (2008). A simplified equation of state for the density of silicate hydrous magmas: An application to the popocatépetl buoyancy-driven dome growth process. *Journal of Volcanology and Geothermal Research*, 171(3):287–300.

[Gunn, 1978] Gunn, D. J. (1978). Transfer of heat or mass to particles in fixed and fluidised beds. *International Journal of Heat and Mass Transfer*, 21(4):467–476.

[Hess and Dingwell, 1996] Hess, K.-U. and Dingwell, D. (1996). Viscosities of hydrous leucogranitic melts: A non-Arrhenian model. *American Mineralogist*, 81:1297–1300.

[Huber et al., 2014] Huber, C., Su, Y., Nguyen, C. T., Parmigiani, A., Gonnermann, H. M., and Dufek, J. (2014). A new bubble dynamics model to study bubble growth, deformation, and coalescence. *Journal of Geophysical Research: Solid Earth*, 119(B1):216–239.

[Hurwitz and Navon, 1994] Hurwitz, S. and Navon, O. (1994). Bubble nucleation in rhyolitic melts: Experiments at high pressure, temperature, and water content. *Earth and Planetary Science Letters*, 122:267–280.

[Jaupart and Allègre, 1991] Jaupart, C. and Allègre, C. J. (1991). Gas content, eruption rate and instabilities of eruption regime in silicic volcanoes. *Earth and Planetary Science Letters*, 102(3):413–429.

[Kozono and Koyaguchi, 2009] Kozono, T. and Koyaguchi, T. (2009). Effects of relative motion between gas and liquid on 1-dimensional steady flow in silicic volcanic conduits: 1. an analytical method. *Journal of Volcanology and Geothermal Research*, 180(1):21–36.

[Kozono and Koyaguchi, 2012] Kozono, T. and Koyaguchi, T. (2012). Effects of gas escape and crystallization on the complexity of conduit flow dynamics during lava dome eruptions. *Journal of Geophysical Research*, 117.

[La Spina and de' Michieli Vitturi, 2012] La Spina, G. and de' Michieli Vitturi, M. (2012). High-resolution finite volume central schemes for a compressible two-phase model. *SIAM Journal on Scientific Computing*, 34(6):B861–B880.

[La Spina et al., 2017] La Spina, G., de' Michieli Vitturi, M., and Clarke, A. (2017). Transient numerical model of magma ascent dynamics: application to the explosive eruptions at the soufrière hills volcano. *Journal of Volcanology and Geothermal Research*, 336:118–139.

[Lensky et al., 2004] Lensky, N., Navon, O., and Lyakhovsky, V. (2004). Bubble growth during decompression of magma: experimental and theoretical investigation. *Journal of Volcanology and Geothermal Research*, 129(1):7 – 22. The role of laboratory experiments in volcanology.

[Lensky et al., 2008] Lensky, N. G., Sparks, R. S. J., Navon, O., and Lyakhovsky, V. (2008). Cyclic activity at Soufrière Hills Volcano, Montserrat: degassing-induced pressurization and stick-slip extrusion. *Geological Society, London, Special Publications*, 307(1):169–188.

[Llewellin et al., 2002] Llewellin, E., Mader, H., and Wilson, S. (2002). The constitutive equation and flow dynamics of bubbly magmas. *Geophysical Research Letters*, 24:2170.

[Lyakhovsky et al., 1996] Lyakhovsky, V., Hurwitz, S., and Navon, O. (1996). Bubble growth in rhyolitic melts: experimental and numerical investigation. *Bulletin of Volcanology*, 58(1):19–32.

[Mancini et al., 2016] Mancini, S., Forestier-Coste, L., Burgisser, A., James, F., and Castro, J. (2016). An expansion–coalescence model to track gas bubble populations in magmas. *Journal of Volcanology and Geothermal Research*, 313:44–58.

[Mason et al., 2006] Mason, R., Starostin, A., Melnik, O., and Sparks, R. (2006). From vulcanian explosions to sustained explosive eruptions: The role of diffusive mass transfer in conduit flow dynamics. *Journal of Volcanology and Geothermal Research*, 153 (1-2):148 – 165. Publisher: Elsevier.

[Massol and Jaupart, 1999] Massol, H. and Jaupart, C. (1999). The generation of gas overpressure in volcanic eruptions. *Earth and Planetary Science Letters*, 166(1):57–70.

[Massol and Jaupart, 2009] Massol, H. and Jaupart, C. (2009). Dynamics of magma flow near the vent: Implications for dome eruptions. *Earth and Planetary Science Letters*, 279(3):185–196.

[Melnik, 2000] Melnik, O. (2000). Dynamics of two-phase conduit flow of high-viscosity gas-saturated magma: large variations of sustained explosive eruption intensity. *Bulletin of Volcanology*, 62(3):153–170.

[Melnik and Sparks, 2005] Melnik, O. and Sparks, R. S. J. (2005). Controls on conduit magma flow dynamics during lava dome building eruptions. *Journal of Geophysical Research: Solid Earth*, 110(B2).

[Michaut et al., 2013] Michaut, C., Ricard, Y., Bercovici, D., and Sparks, R. S. J. (2013). Eruption cyclicity at silicic volcanoes potentially caused by magmatic gas waves. *Nature Geoscience*, 6(10):856–860.

[Mueller et al., 2005] Mueller, S., Melnik, O., Spieler, O., Scheu, B., and Dingwell, D. B. (2005). Permeability and degassing of dome lavas undergoing rapid decompression: An experimental determination. *Bulletin of Volcanology*, 67(6):526–538.

[Mullet and Segall, 2021] Mullet, B. G. and Segall, P. (2021). Stress-Driven Failure of Cylindrical Volcanic Conduits. *Journal of Geophysical Research: Solid Earth*, 126(8):e2021JB022278.

[Musser and Carney, 2020] Musser, J. M. and Carney, J. E. (2020). Theoretical Review of the MFIX Fluid and Two-Fluid Models. Technical Report DOE/NETL-2020/2100, NETL.

[Narbona-Reina et al., 2024] Narbona-Reina, G., Bresch, D., Burgisser, A., and Collombet, M. (2024). Two-phase systems with possible phase exchanges – part i – physical modeling for the evolution of magma in a volcanic conduit. Submitted.

[Ni and Zhang, 2008] Ni, H. and Zhang, Y. (2008). H2o diffusion models in rhyolitic melt with new high pressure data. *Chemical Geology*, 250(1):68–78.

[Papale and Dobran, 1993] Papale, P. and Dobran, F. (1993). Modeling of the ascent of magma during the plinian eruption of vesuvius in a.d. 79. *Journal of Volcanology and Geothermal Research*, 58(1):101–132. Mount Vesuvius.

[Poinsot and Lele, 1992] Poinsot, T. and Lele, S. (1992). Boundary conditions for direct simulations of compressible viscous flows. *Journal of Computational Physics*, 101(1):104–129.

[Rudy and Strikwerda, 1981] Rudy, D. H. and Strikwerda, J. C. (1981). Boundary conditions for subsonic compressible navier-stokes calculations. *Computers and Fluids*, 9(3):327–338.

[Russell et al., 2022] Russell, J. K., Hess, K.-U., and Dingwell, D. B. (2022). Models for viscosity of geological melts. *Reviews in Mineralogy and Geochemistry*, 87(1):841–885.

[Ruth and Ma, 1992] Ruth, D. and Ma, H. (1992). On the derivation of the Forchheimer equation by means of the averaging theorem. *Transport in Porous Media*, 7:255–264.

[Schlichting and Gersten, 2017] Schlichting, H. and Gersten, K. (2017). *Boundary-Layer Theory*. Springer, Berlin, Heidelberg.

[Shea, 2017] Shea, T. (2017). Bubble nucleation in magmas: A dominantly heterogeneous process? *Journal of Volcanology and Geothermal Research*, 343:155–170.

[Slezin, 2003] Slezin, Y. (2003). The mechanism of volcanic eruptions (a steady state approach). *Journal of Volcanology and Geothermal Research*, 122(1-2):7–50.

[Sparks, 1978] Sparks, R. (1978). The dynamics of bubble formation and growth in magmas: A review and analysis. *Journal of Volcanology and Geothermal Research*, 3(1):1–37.

[Su and Huber, 2017] Su, Y. and Huber, C. (2017). The effect of nonlinear decompression history on H2O/CO2 vesiculation in rhyolitic magmas. *Journal of Geophysical Research: Solid Earth*, 122(4):2712–2723.

[Survey et al., 2000] Survey, U. S. G., Mastin, L. G., and Ghiorso, M. S. (2000). A numerical program for steady-state flow of magma-gas mixtures through vertical eruptive conduits. Technical report, USGS, Vancouver, WA.

[Wilson, 1980] Wilson, L. (1980). Relationships between pressure, volatile content and ejecta velocity in three types of volcanic explosion. *Journal of Volcanology and Geothermal Research*, 8:297–313.

[Wilson and Head, 1981] Wilson, L. and Head, J. I. (1981). Ascent and eruption of basaltic magma on the Earth and Moon. *Journal of Geophysical Research*, 86:2971–3001.

[Wilson, 1998] Wilson, S. (1998). A mechanism for the lateral transport of gas bubbles in silicic lava rising in a vertical conduit. *Earth and Planetary Science Letters*, 156:13–18.

[Wong and Segall, 2019] Wong, Y.-Q. and Segall, P. (2019). Numerical analysis of time-dependent conduit magma flow in dome-forming eruptions with application to mount st. helens 2004-2008. *Journal of Geophysical Research: Solid Earth*, 124(11):11251–11273.

[Woods, 1995] Woods, A. W. (1995). The dynamics of explosive volcanic eruptions. *Reviews of Geophysics*, 33(4):495–530.

[Yoshida and Koyaguchi, 1999] Yoshida, S. and Koyaguchi, T. (1999). A new regime of volcanic eruption due to the relative motion between liquid and gas. *Journal of Volcanology and Geothermal Research*, 89:303–315.